Meccanica (2014) 49:2933–2963
DOI 10.1007/s11012-014-0045-4

Energetic versus maximally-dissipative local solutions of a quasi-static rate-independent mixed-mode delamination model

Roman Vodička · Vladislav Mantič · Tomáš Roubíček

Received: 7 November 2013 / Accepted: 16 August 2014 / Published online: 23 September 2014

Abstract A quasi-static rate-independent model of delamination of linearly elastic bodies at small strains, sensitive to mode of delamination, using interfacial damage and interfacial plasticity as two internal parameters, is further developed with the aim to extract representations typically employed in engineering interface-models, i.e. fracture envelope and fracture energy dependence on the mode mixity, which are suitable for the model fitting to experimental data. Moreover, two concepts of solutions are implemented: globally stable energy-conserving solutions or stress-driven maximally-dissipative local solutions, arising by the fully implicit or by a semi-implicit time-stepping procedures, respectively, both yielding numerically stable and convergent time-discretizations. Spatial discretization is performed by the symmetric Galerkin boundary-element method (SGBEM). Alternating quadratic programming is implemented to cope with, respectively, global or local, energy-minimizations in the computation of the time-discretized solutions. Sample 2D numerical examples document applicability of the model as well as efficiency of the SGBEM numerical implementation and facilitate comparison of the two mentioned solution concepts.

Keywords Adhesive contact · Debonding · Interface fracture · Interface damage · Interface plasticity · Imperfect interface · Weak interface · Symmetric Galerkin BEM · Alternating quadratic programming · Local-solution concepts

R. Vodička (✉)
Civil Engineering Faculty, Technical University of Košice, Vysokoškolská 4, 042 00 Košice, Slovakia
e-mail: roman.vodicka@tuke.sk

V. Mantič
School of Engineering, University of Seville, Camino de los Descubrimientos s/n, 41092 Seville, Spain

T. Roubíček
Mathematical Institute, Charles University, Sokolovská 83, 186 75 Praha 8, Czech Republic
e-mail: roubicek@karlin.mff.cuni.cz

T. Roubíček
Institute of Thermomechanics of the ASCR, Dolejškova 5, 182 00 Praha 8, Czech Republic

1 Introduction

Number of applications of layered and laminated structures is increasing recently, an example being applications of composite materials extensively used in aircraft industry nowadays, where powerful numerical methods to characterize damage initiation and propagation are required, e.g. [2]. In particular, the problem of interface cracks initiation and propagation is fundamental in the analysis of these structures. Therefore, development and investigation of relevant mathematical models of interface damage and fracture seems to be very important. In many situations, the

interface between bulk subdomains, usually represented by a relatively thin adhesive layer, can be partially or completely damaged. We model this layer as infinitesimally thin, speaking thus about a *delaminating interface*. This situation is usually referred to as delamination—debonding of adjacent material bodies.

There are several possibilities to describe the interface damage by energy-based principles. The present model follows Frémond's approach [19] and defines a scalar damage (or *delamination*) *variable* along the interface, cf. also [20, 25, 47] and references therein. Along with this variable, an energy formulation governing the adhesive damage until it breaks is proposed. The proposed energy functionals include not only the energy stored in the adjacent bulk subdomains and in the adhesive interface but also the dissipated energy. The inelastic delamination process can be very fast comparing to the typical rate of outer loading, and then this dissipation (in particular also in the aforementioned references) can and will be described as a reasonable approximation of a rate-independent process.

From the physical point of view, the dissipation of energy at an interface can be of a different nature. The first one, given by the damage of the adhesive interface during the loading process applied, has already been mentioned above. However, this rather simple formulation does not include all the physical phenomena that can take place at an interface. During the damage process in this (infinitesimally) thin adhesive layer, the growing cracks can be loaded in pure opening or shear mode (Mode I or II, respectively), or in mixed mode. In order to provide a better reflection of the experimental results, another interface variable is included in the present model to reflect an increase of the fracture toughness in the Mode II. This variable represents plastic tangential slip along the interface describing some plastification in the adhesive before the debonding of the adjacent bulk subdomains [38, 44, 47, 48]. Related models including plasticity at the interface were developed and studied, sometimes also experimentally verified, in [16, 21, 22, 27, 32, 37, 50, 55, 63]. Another dissipative process which can take place at the interface is friction. Here, after delamination, however, only simple frictionless contact is considered for the sake of simplicity; see [1, 54] for interface models including friction.

We consider *small strains* and *isotropic*, piecewise *homogeneous* and *linearly responding material* and neglect in particular inertia, viscosity, and any temperature-dependent effects. Therefore, in particular, the elastic state of the adjacent bulk subdomains is governed by systems of linear partial differential equations and can be analyzed by any suitable numerical technique, typically finite- or also boundary-element methods (FEM or BEM, respectively). Here, the *symmetric Galerkin boundary element method* (SGBEM) [7, 49, 52, 57] is applied to the above introduced delamination (or debonding) problems. SGBEM enables a natural derivation by means of an energy-based formulation [6, 7, 61, 62] which is its principal advantage in the present approach to characterize the damage and failure of an adhesive interface.

The numerical treatment of the solution process includes as a crucial part an algorithm for finding the global or (some specific) local minima of incremental problems. This kind of damage-type problems ultimately leads to a generally non-convex mathematical programming. In the present implementation, an alternating minimization algorithm (AMA) is designed to split the solution to a series of quadratic-programming calculations. The algorithms for this kind of solutions can effectively be based on conjugate gradient schemes [17], which were successfully implemented in the present work.

The plan of this paper is the following: In Sect. 2, we introduce the model involving interface damage and plasticity and make its certain fitting to a conventional engineering model. A computer implementation of the two solution concepts related to two numerical stable ways of time discretization for this model is presented in Sect. 3. Eventually, in Sect. 4, the proposed approaches are also tested numerically in two examples to demonstrate the behavior of the model and to assess its suitability in a particular physical situation.

2 A model involving interface plasticity and damage

For the sake of simplicity, only 2D problems will be considered in the present work. Let a body be defined by a bounded planar domain $\Omega \subset \mathbb{R}^2$ with boundary $\partial\Omega = \Gamma$.

The domain Ω consists of several subdomains Ω^η. For the sake of simplicity, only two non-overlapping subdomains Ω^{A} and Ω^{B} with Lipschitz boundaries

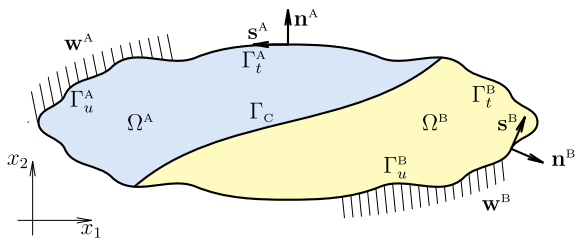

Fig. 1 Model of debonding of two subdomains

$\Gamma^{\mathrm{A}} = \partial\Omega^{\mathrm{A}}$ and $\Gamma^{\mathrm{B}} = \partial\Omega^{\mathrm{B}}$ will be considered hereinafter, cf. Fig. 1. Let $\mathbf{n}^{\eta}$ denote the unit outward normal vector defined a.e. at Γ^{η} and let $\mathbf{s}^{\eta}$ denote the unit tangential anticlockwise oriented vector.

The common part of Γ^{A} and Γ^{B}, called interface, is denoted as $\Gamma_{\mathrm{C}} = \Gamma^{\mathrm{A}} \cap \Gamma^{\mathrm{B}}$. Dirichlet boundary conditions defined on a part of the outer boundary represent a hard-device loading, prescribing displacements $\mathbf{u} = \mathbf{w}$ at Γ_u^{A} and Γ_u^{B}. Homogenous Neumann boundary conditions are defined on the remaining traction free part of the outer boundaries, denoted as Γ_t^{A} and Γ_t^{B}, prescribing tractions $\mathbf{t} = \mathbf{0}$. Thus, we consider $\Gamma^{\eta} = \overline{\Gamma_u^{\eta}} \cup \overline{\Gamma_t^{\eta}} \cup \overline{\Gamma_{\mathrm{C}}}$ (overline denoting closure of a set), where $\eta = \mathrm{A}, \mathrm{B}$, with $\overline{\Gamma_u^{\eta}} \cap \overline{\Gamma_{\mathrm{C}}} = \emptyset$, and obviously $\Gamma_u^{\eta} \cap \Gamma_t^{\eta} = \Gamma_t^{\eta} \cap \Gamma_{\mathrm{C}} = \emptyset$.

2.1 Stored and dissipated energy functionals governing the model

The interface Γ_{C} is considered as an infinitesimally thin adhesive layer represented by a continuous spring distribution with normal and tangential elastic stiffnesses $k_{\mathbf{n}}$ and $k_{\mathbf{s}}$, respectively. It is considered that the subdomains can debond along the interface Γ_{C}, this debonding process being considered as rate-independent. During this process the material of the adhesive layer is damaged. This is modelled by a scalar damage variable ζ which varies at each interface point between one and zero: value one and zero, respectively, corresponding to undamaged and fully damaged adhesive at a particular point. In addition to this variable, a plastic tangential slip variable π is considered at the interface which allows for making a difference between fracture Mode I and II in the following sense: some additional dissipated energy is associated to interface fracture in Mode II in agreement with experimental observations of interface crack growth, where the energy dissipated in Mode II is significantly greater than that dissipated in Mode I and also correspondingly the associated plastic zones in the adjacent bulk are larger in Mode II than in Mode I. It is expected that the interface plastic behaviour considered in the present work represents a useful and practical approximation of the plastic phenomena associated to relatively narrow plastic zones in the bulk located in the interface vicinity. Let us remark that the idea of the interfacial plasticity can be used in adhesive contact modelling also for different purposes than mode-sensitivity, namely fatigue, cf. [51].

Let us consider the energy stored [25, 46, 47] in the structure (given by $\Omega^{\mathrm{A}}, \Omega^{\mathrm{B}}$ and Γ_{C}) obeying the aforementioned type of interface damage and kinematic-hardening-plasticity model [44], with the plastic slope k_{H}, as

$$\mathcal{E}(t,\mathbf{u},\zeta,\pi) = \begin{cases} \displaystyle\int_{\Gamma^{\mathrm{A}}} \frac{1}{2}\mathbf{u}^{\mathrm{A}} \cdot \mathbf{t}^{\mathrm{A}}(\mathbf{u}^{\mathrm{A}})\,\mathrm{d}S + \int_{\Gamma^{\mathrm{B}}} \frac{1}{2}\mathbf{u}^{\mathrm{B}} \cdot \mathbf{t}^{\mathrm{B}}(\mathbf{u}^{\mathrm{B}})\,\mathrm{d}S \\ \displaystyle + \int_{\Gamma_{\mathrm{C}}} \frac{1}{2}\left[\zeta\left(k_{\mathbf{n}}[\mathbf{u}]_n^2 + k_{\mathbf{s}}\left([\mathbf{u}]_{\mathbf{s}} - \pi\right)^2\right) + k_{\mathrm{H}}\pi^2 + k_0|\nabla_{\mathbf{s}}\zeta|^2 + k_1|\nabla_{\mathbf{s}}\pi|^2\right]\mathrm{d}S \quad \text{if } \mathbf{u}^{\eta} = \mathbf{w}^{\eta}(t) \text{ on } \Gamma_u^{\eta}, \text{and} \\ \qquad\qquad \text{if } [\mathbf{u}]_n \geq 0 \,\&\, 0 \leq \zeta \leq 1 \text{ on } \Gamma_{\mathrm{C}}, \\ +\infty, \qquad\qquad \text{elsewhere.} \end{cases} \tag{1}$$

The first two integrals, representing the elastic strain energy in the bulk (adjacent subdomains Ω^{η}), are

expressed in their boundary form (taking into account that $\mathbf{t}^\eta = \mathbf{t}^\eta(\mathbf{u}^\eta)$), which is advantageous when the numerical technique for solving elastic problems in Ω^η is also boundary based. The first condition on Γ_C is the Signorini condition of the unilateral contact, where the relative normal displacement $[\mathbf{u}]_n = (\mathbf{u}^B - \mathbf{u}^A)\cdot\mathbf{n}^A$ is introduced. Similarly, the relative tangential displacement (or slip) $[\mathbf{u}]_s$ is defined $[\mathbf{u}]_s = (\mathbf{u}^B - \mathbf{u}^A)\cdot\mathbf{s}^A$.

The gradient terms are added to the functional in a similar way as it is usual in the gradient theory of damage or plasticity, see [20]. It includes some nonlocal effect to the internal parameters and facilitates the mathematical treatment of the model [47]. The parameters k_0 and k_1 are usually assumed small, determining a certain length-scale of possible oscillation of ζ and π, respectively, along Γ_C. Note that, in the present 2D case, the surface gradients $\nabla_s\zeta$ and $\nabla_s\pi$ reduce to the tangential derivatives with respect to Γ_C.

The dissipation potential for a rate-independent process can be represented by a degree-1 homogeneous functional [36]. Considering both processes of the interface damage and of the plastic slip, the interface dissipation potential is given as follows:

$$\mathcal{R}(\dot\zeta,\dot\pi) = \begin{cases} \displaystyle\int_{\Gamma_C} \left(G_d|\dot\zeta| + \sigma_{\text{yield}}|\dot\pi|\right) \mathrm{d}S & \text{if } \dot\zeta \le 0 \text{ on } \Gamma_C, \\ +\infty, & \text{elsewhere.} \end{cases} \tag{2}$$

The rates of the damage and the plastic slip are denoted by $\dot\zeta$ and $\dot\pi$, respectively; e.g. $\dot\zeta = \frac{\partial\zeta}{\partial t}$. The parameter G_d is the (minimum) interface fracture energy (sometimes called activation energy) required to a complete damage (debond) of a unit of area of the interface following the linear elastic-purely brittle part of the interface constitutive law. In particular, G_d represents the interface fracture energy in Mode I. Moreover, σ_{yield} is the interface yield (shear) stress for initiation of the plastic slip along the interface.

The rate-independent evolution is governed by the initial-value problem for the system of nonlinear variational inclusions

$$\partial_{\mathbf{u}}\mathcal{E}(t,\mathbf{u},\zeta,\pi) \ni 0, \quad \mathbf{u}(0) = \mathbf{u}_0, \tag{3a}$$

$$\partial_{\dot\zeta}\mathcal{R}(\dot\zeta) + \partial_\zeta\mathcal{E}(t,\mathbf{u},\zeta,\pi) \ni 0, \quad \zeta(0) = \zeta_0, \tag{3b}$$

$$\partial_{\dot\pi}\mathcal{R}(\dot\pi) + \partial_\pi\mathcal{E}(t,\mathbf{u},\zeta,\pi) \ni 0, \quad \pi(0) = \pi_0, \tag{3c}$$

where the symbol ∂ refers to partial subdifferential relying on convexity of pertinent functionals with respect to each particular variable, see [47], and where we already reflected that $\partial_{\dot\pi}\mathcal{R}$ is independent of $\dot\zeta$ and that $\partial_{\dot\zeta}\mathcal{R}$ is independent of $\dot\pi$. Note that, in fact, $\mathbf{u}_0$ is here uniquely determined by ζ_0 and π_0 through $\partial_{\mathbf{u}}\mathcal{E}(0,\mathbf{u}_0,\zeta_0,\pi_0)\ni 0$. Note also that here all involved functionals are indeed non-smooth due to the absolute values and unidirectional constraint in (2) or Signorini unilateral and the ζ- constraints in (1). Recall that the subdifferential $\partial\mathcal{F}(\mathbf{w})$ of an 'energy' functional $\mathcal{F}(\mathbf{w})$ at $\mathbf{w}$ is a set of 'forces' (dual quantities) $\mathbf{F}$, such that for the 'work' $\langle\mathbf{F},\mathbf{w}\rangle$ the inequality holds $\langle\mathbf{F},\mathbf{v}-\mathbf{w}\rangle + \mathcal{F}(\mathbf{w}) \le \mathcal{F}(\mathbf{v})$ for any appropriate $\mathbf{v}$. Thus, vanishing $\mathbf{F}$ provides the first-order optimality condition for the minimization of $\mathcal{F}$.

It should be stressed that the definition of local-solution concept to the initial-value problem (3) introduced in Sect. 2.3 below involves the time derivative of stored energy $\frac{\partial}{\partial t}\mathcal{E}$ in (24a) which is hardly defined for time-dependent boundary condition in (1). Hence, using an additive shift of displacement $\mathbf{u}$ by an appropriate extension of $\mathbf{w}$ to obtain homogeneous boundary conditions as described e. g. in [44, 47] is required to give a sense to $\frac{\partial}{\partial t}\mathcal{E}$ for a transformed $\mathcal{E}$; we omit details about this standard transformation. Here, if Γ_C and Γ_u^η are far from each other, one can alternatively benefit from usage of BEM in Sect. 3.3 below to reformulate (24) only in terms of values of $\mathbf{u}$ on Γ_C and thus to eliminate simply the time-dependent constraints on Γ_u^η; again we omit details.

2.2 Interface constitutive law—engineering insight

The present interface model can be described in terms of the *energy release rate* (ERR). In the linear elastic interface model [12, 14, 28], the ERR at the crack tip can be shown to be defined as the elastic strain energy per unit area stored in the 'spring' located at the crack-tip prior to failure. Although, the following derivation is carried out having in mind this 'spring' at the crack tip, in fact they are valid for any other undamaged 'spring'.

An engineering insight into the present interface constitutive law can be summarized by the two conditions which activate two inelastic processes included in the formulation. The first one is the activation criterion for initiation of debonding (interface

damage) which can be derived from the condition (3b) considering only the crack-tip spring. It reads

$$\frac{1}{2}\left(k_{\mathbf{n}}u_{\mathbf{n}}^2+k_{\mathbf{s}}(u_{\mathbf{s}}-\pi)^2\right)\leq G_{\mathrm{d}}+\mathrm{div}_{\mathbf{s}}\left(k_0\nabla_{\mathbf{s}}\zeta\right), \tag{4a}$$

where $u_{\mathbf{n}}=[\mathbf{u}]_n\geq 0$ and $u_{\mathbf{s}}=[\mathbf{u}]_s$ represent the elongation of the spring in the normal and tangential directions, respectively. The last term effectively modifies the threshold G_{d} according the variation of the damage profile in a vicinity of a current point, realizing thus nonlocal hardening/weakening-like effects. In fact, the form of this term in (4a) holds only on a flat Γ_{C} while on a curved boundary a more complicated form arises from (3b) with (1). Of course, (3b) itself represents the complementarity problem which, together with (4a), involves still

$$\dot{\zeta}\leq 0 \text{ and } \dot{\zeta}\left(\frac{1}{2}\left(k_{\mathbf{n}}u_{\mathbf{n}}^2+k_{\mathbf{s}}(u_{\mathbf{s}}-\pi)^2\right)-G_{\mathrm{d}}-\mathrm{div}_{\mathbf{s}}(k_0\nabla_{\mathbf{s}}\zeta)\right)=0. \tag{4b}$$

The complementarity problem (4) is to be valid on Γ_{C}. Actually, we wrote it for simplicity for $\zeta>0$ while, in general, it still should involve the multiplier to the constraint $\zeta\geq 0$ while the constraint $\zeta\leq 1$ in (1) can be assumed nonactive due to the constraint $\dot{\zeta}\leq 0$ in (2) if the initial condition satisfies it, i.e. if $\zeta_0\leq 1$.

The evolution of the interface plastic slip π is analogous with the evolution of plastic strain in the conventional plasticity. The condition for evolution of plastic slip can be derived from (3c) which provides the following inequality for the crack-tip spring

$$\left|\zeta k_{\mathbf{s}}(u_{\mathbf{s}}-\pi)-k_{\mathrm{H}}\pi+\mathrm{div}_{\mathbf{s}}\left(k_1\nabla_{\mathbf{s}}\pi\right)\right|\leq\sigma_{\mathrm{yield}} \tag{5a}$$

assuming again that Γ_{C} is flat. In fact, the classical formulation of (3c) provides, likewise in the case of (4), the complementarity problem which completes (5a) still by

$$\forall\,|\sigma|\leq\sigma_{\mathrm{yield}}:\quad \dot{\pi}\cdot\left(\sigma-\zeta k_{\mathbf{s}}(u_{\mathbf{s}}-\pi)-k_{\mathrm{H}}\pi+\mathrm{div}_{\mathbf{s}}\left(k_1\nabla_{\mathbf{s}}\pi\right)\right)\leq 0. \tag{5b}$$

Thus, due to (5a), π starts or restarts evolving when the tangential driving stress reaches the yield threshold σ_{yield}. Hence, in the positive direction of the tangential displacement we have

$$\zeta k_{\mathbf{s}}(u_{\mathbf{s}}-\pi)-k_{\mathrm{H}}\pi=\sigma_{\mathrm{yield}}-\mathrm{div}_{\mathbf{s}}\left(k_1\nabla_{\mathbf{s}}\pi\right). \tag{6}$$

Disregarding the influence of the gradient terms for more lucid explanation of the essence of functioning of the model, more detailed analysis of the interface constitutive law, in particular schematic traction-displacement plots, can be found in [44], here we only mention one important relation of the material characteristics for the model to produce the desired effects, namely:

$$\frac{1}{2}\sqrt{2k_{\mathbf{s}}G_{\mathrm{d}}}<\sigma_{\mathrm{yield}}\leq\sqrt{2k_{\mathbf{s}}G_{\mathrm{d}}}. \tag{7}$$

The upper bound of the yield stress is necessary for making possible to initiate plastic slip before the total interface damage. The lower bound is required to avoid plastic slip evolution, governed by (5), after debonding ($\zeta=0$). Actually, satisfaction of inequalities in (7) is not strictly necessary for the above model to work, c.f. [44]. If the right-hand side inequality is not fulfilled, i.e. σ_{yield} is too high with respect to G_{d}, then, as could be expected, the model response will be brittle and insensitive to fracture mode mixity and no plastic slip will appear before the interface breakage. If the left-hand-side inequality in (7) is not fulfilled, i.e. the maximum shear stress is larger than $2\sigma_{\mathrm{yield}}$, then, for a back stress $k_{\mathrm{H}}|\pi|>\sigma_{\mathrm{yield}}$, a portion of the hardening energy, specifically $\frac{1}{2}k_{\mathrm{H}}(\pi^2-\pi_*^2)$ (denoting $\pi_*=\sigma_{\mathrm{yield}}/k_{\mathrm{H}}$), will be released at complete unloading. In such a case, the expression of the hardening energy $\frac{1}{2}k_{\mathrm{H}}\pi^2$ in (1) should be replaced by a new expression $\frac{1}{2}k_{\mathrm{H}}\left(\zeta\langle\pi^2-\pi_*^2\rangle_+-\langle\pi^2-\pi_*^2\rangle_-+\pi_*^2\right)$, where $\langle\cdot\rangle_\pm$ denotes the positive and negative part of a real number, in order to account for the released part of hardening energy. Note that, if the left-hand-side inequality in (7) is fulfilled, which is assumed in the present work for the sake of simplicity, then π does not vary at unloading and no portion of the hardening energy is released at complete unloading, which explains why its expression in (1) is not multiplied by ζ.

Hereinafter, some aspects of this interface constitutive law not discussed in [44] will be presented.

In what follows, elongation and energy description of a particular spring rupture are summarized considering fracture mode mixity. The ERR of a mixed-mode crack is thus defined depending on the existence of plastic slip in the interface as

$$G(u_{\mathbf{n}},u_{\mathbf{s}},\pi)=\frac{1}{2}k_{\mathbf{n}}u_{\mathbf{n}}^2+\frac{1}{2}k_{\mathbf{s}}(u_{\mathbf{s}}-\pi)^2+\sigma_{\mathrm{yield}}\pi+\frac{1}{2}k_{\mathrm{H}}\pi^2, \tag{8}$$

which simplifies for $\pi = 0$ to the well-known expression $G(u_{\mathbf{n}}, u_{\mathbf{s}}) = \frac{1}{2}k_{\mathbf{n}}u_{\mathbf{n}}^2 + \frac{1}{2}k_{\mathbf{s}}u_{\mathbf{s}}^2$. In uploading, $\pi = 0$ if $|u_{\mathbf{s}}| \leq \frac{\sigma_{\text{yield}}}{k_{\mathbf{s}}}$. Eliminating the plastic slip π which can be expressed in the simple kinematic-hardening model as, assuming $u_{\mathbf{s}} \geq \frac{\sigma_{\text{yield}}}{k_{\mathbf{s}}}$,

$$\pi = \frac{k_{\mathbf{s}}}{k_{\mathbf{s}} + k_{\text{H}}}\left(u_{\mathbf{s}} - \frac{\sigma_{\text{yield}}}{k_{\mathbf{s}}}\right), \tag{9}$$

the substitution leads to the relation

$$G(u_{\mathbf{n}}, u_{\mathbf{s}}) = \frac{1}{2}k_{\mathbf{n}}u_{\mathbf{n}}^2 + \frac{1}{2}\frac{k_{\mathbf{s}}k_{\text{H}}}{k_{\mathbf{s}} + k_{\text{H}}}\left(u_{\mathbf{s}} + \frac{\sigma_{\text{yield}}}{k_{\text{H}}}\right)^2 - \frac{\sigma_{\text{yield}}^2}{2k_{\text{H}}}, \tag{10}$$

when some interface plasticity evolves. Alternatively, the relation can be expressed in terms of the pertinent stresses $\sigma_{\mathbf{n}} = k_{\mathbf{n}}u_{\mathbf{n}} \geq 0$ and $\sigma_{\mathbf{s}} = k_{\mathbf{s}}(u_{\mathbf{s}} - \pi)$ as

$$G(\sigma_{\mathbf{n}}, \sigma_{\mathbf{s}}) = \frac{\sigma_{\mathbf{n}}^2}{2k_{\mathbf{n}}} + \frac{1}{2}\frac{(k_{\mathbf{s}} + k_{\text{H}})\sigma_{\mathbf{s}}^2}{k_{\mathbf{s}}k_{\text{H}}} - \frac{\sigma_{\text{yield}}^2}{2k_{\text{H}}}. \tag{11}$$

As follows from (1), (2) and (3b) the relation of the interface breakage is unique, when written in terms of stresses, independently of the presence of interface plasticity, namely:

$$\frac{\sigma_{\mathbf{n}}^2}{2k_{\mathbf{n}}} + \frac{\sigma_{\mathbf{s}}^2}{2k_{\mathbf{s}}} = G_{\text{d}}. \tag{12}$$

Nevertheless, it should be noted that at the interface breakage without or with interface plasticity, it holds

$$\begin{aligned} &\frac{1}{2}k_{\mathbf{n}}u_{\mathbf{n}}^2 + \frac{1}{2}k_{\mathbf{s}}u_{\mathbf{s}}^2 = G_{\text{d}}, \text{ or} \\ &\frac{1}{2}k_{\mathbf{n}}u_{\mathbf{n}}^2 + \frac{1}{2}k_{\mathbf{s}}\left(\frac{k_{\text{H}}}{k_{\mathbf{s}} + k_{\text{H}}}\right)^2\left(u_{\mathbf{s}} + \frac{\sigma_{\text{yield}}}{k_{\text{H}}}\right)^2 = G_{\text{d}}, \end{aligned} \tag{13}$$

respectively. Finally, ERR G pertinent to either mode of crack ($G = G_{\text{I}} + G_{\text{II}}$) can be considered as:

$$G_{\text{I}} = \frac{1}{2}k_{\mathbf{n}}u_{\mathbf{n}}^2 = \frac{\sigma_{\mathbf{n}}^2}{2k_{\mathbf{n}}}, \tag{14}$$

and then, without or with interface plasticity,

$$\begin{aligned} G_{\text{II}} &= \frac{1}{2}k_{\mathbf{s}}u_{\mathbf{s}}^2 = \frac{\sigma_{\mathbf{s}}^2}{2k_{\mathbf{s}}}, \text{ resp.} \\ G_{\text{II}} &= \frac{1}{2}\frac{k_{\mathbf{s}}k_{\text{H}}}{k_{\mathbf{s}} + k_{\text{H}}}\left(u_{\mathbf{s}} + \frac{\sigma_{\text{yield}}}{k_{\text{H}}}\right)^2 - \frac{\sigma_{\text{yield}}^2}{2k_{\text{H}}} \\ &= \frac{1}{2}\frac{(k_{\mathbf{s}} + k_{\text{H}})\sigma_{\mathbf{s}}^2}{k_{\mathbf{s}}k_{\text{H}}} - \frac{\sigma_{\text{yield}}^2}{2k_{\text{H}}}, \end{aligned} \tag{15}$$

the latter depending on the presence of the interface plasticity. The relations of the interface breakage, without or with interface plasticity, are then

$$\begin{aligned} &G_{\text{I}} + G_{\text{II}} = G_{\text{d}}, \text{ resp.} \\ &G_{\text{I}} + \frac{k_{\text{H}}}{k_{\mathbf{s}} + k_{\text{H}}}G_{\text{II}} + \frac{\sigma_{\text{yield}}^2}{2(k_{\mathbf{s}} + k_{\text{H}})} = G_{\text{d}}. \end{aligned} \tag{16}$$

The equations in (13) define the relation between the normal and tangential displacements at the crack tip leading to the crack growth. This relation can be visualized as an interface fracture envelope. Similarly, the fracture envelope can be obtained in terms of stresses from the relation (12) and in terms of ERR from (16).

To this end, let us first parameterize the curve of pairs $(u_{\mathbf{n}}, u_{\mathbf{s}})$ corresponding to the crack growth. Before the initiation of interface plasticity ($\pi = 0$) and for no previous damage ($\zeta = 1$), according to $(13)_1$, the parameterization reads as

$$\begin{aligned} &u_{\mathbf{n}} = \sqrt{\frac{2G_{\text{d}}}{k_{\mathbf{n}}}}\cos\varphi, \quad u_{\mathbf{s}} = \sqrt{\frac{2G_{\text{d}}}{k_{\mathbf{s}}}}\sin\varphi, \\ &\text{for} \quad 0 \leq \varphi \leq \arcsin\frac{\sigma_{\text{yield}}}{\sqrt{2k_{\mathbf{s}}G_{\text{d}}}}, \end{aligned} \tag{17a}$$

which is a part of ellipse with the center at the origin. Similarly, after an interface plasticity initiation the relation $(13)_2$ provides another part of the parameterization

$$\begin{aligned} &u_{\mathbf{n}} = \sqrt{\frac{2G_{\text{d}}}{k_{\mathbf{n}}}}\cos\varphi, \quad u_{\mathbf{s}} = \sqrt{\frac{2G_{\text{d}}}{k_{\mathbf{s}}}}\frac{k_{\mathbf{s}} + k_{\text{H}}}{k_{\text{H}}} \\ &\times \sin\varphi - \frac{\sigma_{\text{yield}}}{k_{\text{H}}}, \quad \text{for} \quad \arcsin\frac{\sigma_{\text{yield}}}{\sqrt{2k_{\mathbf{s}}G_{\text{d}}}} \leq \varphi \leq \frac{\pi}{2}. \end{aligned} \tag{17b}$$

Though, this corresponds to a parameterization of a different ellipse, whose center is at the point

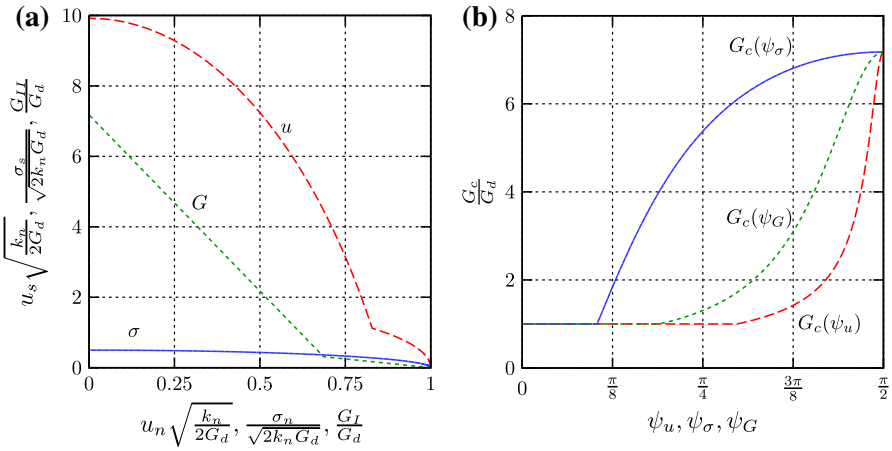

Fig. 2 **a** Dimensionless interface fracture envelopes in terms of relative displacements (*two ellipses*), stresses (*one ellipse*) or ERR components (a *broken line*) and **b** fracture energy G_c as a function of fracture mode-mixity angles, for $G_d = 10$ J/m^2, $k_n = 18$ TPa/m, $\sigma_{yield} = 0.79\sqrt{k_s G_d}$, $k_s = k_n/4$, $k_H = k_s/9$

$(0, -\frac{\sigma_{yield}}{k_H})$, the parameter φ continuously switches from a state without plasticity to a state with an interface plastic slip.

Let us now parameterize the curve of pairs (σ_n, σ_t) corresponding to the interface breakage. As long as it is a part of an ellipse, the parameterization reads

$$\sigma_n = \sqrt{2k_n G_d}\cos\varphi, \quad \sigma_s = \sqrt{2k_s G_d}\sin\varphi. \tag{18}$$

In fact, the angle φ in the parameterizations (17) and in the relation (18) is the same.

Finally, the relations (16) provide the curve of pairs (G_I, G_{II}) as a broken line. All three graphs for a particular choice of material parameters, used in the numerical example in Sect. 4, are shown in Fig. 2a.

The fracture mode-mixity angle of an interface crack can generally be introduced in three ways, see [59], based on the crack-tip displacements, crack-tip stresses or ERR components, respectively,

$$\psi_u = \arctan\frac{u_s}{u_n}, \qquad \psi_\sigma = \arctan\frac{\sigma_s}{\sigma_n}, \qquad \psi_G = \arctan\sqrt{\frac{G_{II}}{G_I}}. \tag{19}$$

It is assumed that a crack propagates if the ERR G reaches the fracture energy G_c, i.e. $G = G_c(\psi), \psi$ denoting one of the mode-mixity angles in (19). It means that if crack grows before interface plasticity appears, $G_d = G_c$. However, in presence of some interface plasticity these two quantities separate. Let us try to find the relation $G_c = G_c(\psi)$.

Both relations $G_c = G_c(\psi_u)$ and $G_c = G_c(\psi_\sigma)$, for the case of interface plasticity, can be obtained from $G = G_I + G_{II}$ in (12) and the expression $(15)_2$ substituting (18), because φ in relations (17) and (18) is the same. This renders

$$\begin{aligned}\frac{\sigma_n^2}{2k_n} + \frac{1}{2}\frac{(k_s+k_H)\sigma_s^2}{k_s k_H} - \frac{\sigma_{yield}^2}{2k_H} &= G_d\cos^2\varphi + \frac{(k_s+k_H)G_d\sin^2\varphi}{k_H} - \frac{\sigma_{yield}^2}{2k_H}\\ &= G_d\left(1 + \frac{k_s}{k_H}\sin^2\varphi\right) - \frac{\sigma_{yield}^2}{2k_H} = G_c(\varphi).\end{aligned} \tag{20}$$

The relation $\varphi = \varphi(\psi_u)$ can be obtained from

$$\tan\psi_u = \sqrt{\frac{k_n}{k_s}}\frac{k_s+k_H}{k_H}\tan\varphi - \sqrt{\frac{k_n}{2G_d}}\frac{\sigma_{yield}}{k_H}\frac{1}{\cos\varphi} \tag{21}$$

which can be substituted into (20). The final relation is, however, somewhat cumbersome preventing from writing explicitly an expression of $G_c(\psi_u)$. Nevertheless, the graph of $G_c = G_c(\psi_u)$ can easily be plotted, see Fig. 2b.

The relation $\tan\varphi = \tan\varphi(\psi_\sigma) = \sqrt{\frac{k_n}{k_s}}\tan(\psi_\sigma)$, obtained by comparing $(19)_2$ and (18), can be easily substituted into (20). The resulting relation $G_c = G_c(\psi_\sigma)$ is

$$G_d\left(1 + \frac{k_s}{k_H}\frac{k_H\tan^2\psi_\sigma}{k_s + k_H\tan^2\psi_\sigma}\right) - \frac{\sigma_{yield}^2}{2k_H} = G_c(\psi_\sigma). \tag{22}$$

Finally, deducing the corresponding expression related to ERR is also straightforward. It is sufficient to express both G_I and G_{II} from the system $(16)_2$ and $(19)_3$

$$G_{\mathrm{I}}+G_{\mathrm{II}}=G_{\mathrm{I}}\big(1+\tan^2\psi_G\big)=\frac{2G_{\mathrm{d}}(k_{\mathbf{s}}+k_{\mathrm{H}})-\sigma_{\mathrm{yield}}^2}{2(k_{\mathbf{s}}+k_{\mathrm{H}}+k_{\mathrm{H}}\tan^2\psi_G)}\big(1+\tan^2\psi_G\big)=G_{\mathrm{c}}(\psi_G),\tag{23}$$

which is valid for $\arcsin\frac{\sigma_{\mathrm{yield}}}{\sqrt{2k_{\mathbf{s}}G_{\mathrm{d}}}}\le\psi_G\le\frac{\pi}{2}$, whereas $G_{\mathrm{c}}(\psi_G)=G_{\mathrm{d}}$ for smaller ψ_G. Dependence of the fracture energy G_{c} on all the types of mode-mixity angles are plotted in Fig. 2b. A nice qualitative agreement with experimental results in [3, 18, 24, 26, 29, 58], see also [30] and further references therein, can be observed. Actually, the above fracture envelopes and fracture energy dependence on mode mixity can be used in practical fitting of the present model to experimental data for a particular interface.

2.3 Two local-solution concepts: energy (ES) versus stress (MDLS)

Relying on homogeneity of degree 1 of the functional $\mathcal{R}$, both with respect to $\dot\zeta$ and $\dot\pi$, the "weak formulation" of the initial-value problem (3) was essentially devised just for the delamination-type problems in [56, 60], cf. also [33], by the following definition: the triple $(\mathbf{u},\zeta,\pi)$ is called a *local solution* to (3) if the following four properties are satisfied:

(i) *Energy imbalance:* For all $0\le t_1\le t_2\le T$:

$$\mathcal{E}(t_2,\mathbf{u}(t_2),\zeta(t_2),\pi(t_2))+\mathrm{Diss}_{\mathcal{R}}(\zeta,\pi;[t_1,t_2])\le\int_{t_1}^{t_2}\frac{\partial}{\partial t}\mathcal{E}(t,\mathbf{u}(t),\zeta(t),\pi(t))\mathrm{d}t+\mathcal{E}(t_1,\mathbf{u}(t_1),\zeta(t_1),\pi(t_1))\tag{24a}$$

with $\mathrm{Diss}_{\mathcal{R}}(\zeta,\pi;[t_1,t_2])=\sup_{t_1\le s_0<\ldots<s_n\le t_2}\sum_{j=1}^{N}\mathcal{R}\big(\zeta(s_j)-\zeta(s_{j-1}),\,\pi(s_j)-\pi(s_{j-1})\big)$,

(ii) *Variation inequality for displacement* $\mathbf{u}$: For a.a. $t\in[0,T]$:

$$\forall\,\tilde{\mathbf{u}}:\quad\mathcal{E}(t,\mathbf{u}(t),\zeta(t),\pi(t))\le\mathcal{E}(t,\tilde{\mathbf{u}},\zeta(t),\pi(t)),\tag{24b}$$

(iii) *Semi-stability for* ζ *and* π: For a.a. $t\in[0,T]$:

$$\forall\,\tilde\zeta:\quad\mathcal{E}(t,\mathbf{u}(t),\zeta(t),\pi(t))\le\mathcal{E}(t,\mathbf{u}(t),\tilde\zeta,\pi(t))+\mathcal{R}(\tilde\zeta-\zeta(t),0),\tag{24c}$$

$$\forall\,\tilde\pi:\quad\mathcal{E}(t,\mathbf{u}(t),\zeta(t),\pi(t))\le\mathcal{E}(t,\mathbf{u}(t),\zeta(t),\tilde\pi)+\mathcal{R}(0,\tilde\pi-\pi(t)),\tag{24d}$$

(iv) *Initial conditions*

$$\mathbf{u}(0)=\mathbf{u}_0,\ \ \zeta(0)=\zeta_0,\ \ \pi(0)=\pi_0.\tag{24e}$$

Actually, here we combined the original local-solution concept [56, 60] with the concept of semi-stability [40]. From the viewpoint of applications, it is important that the energy imbalance (24a) is formulated as an inequality, which allows for modelling ruptures that intentionally do not jump unphysically early (or in unphysically less dissipative modes) and inevitably do not conserve energy, as demonstrated in particular in this paper. The possible energy gap thus arising can be understood due to neglected viscous dissipative mechanisms, cf. also [45], or neglected elastic waves, whereas in a quasistatic and rate-independent problem formulation it can be associated to a snap-back instability originating a crack jump, cf. [11, 31].

It can be shown that, under mild qualification assumptions on the problem (satisfied in our case), the local solutions are just conventional weak (but not strong!) solutions to (3), cf. [43, Prop. 2.3]. If $\mathcal{E}(t,\cdot)$ is convex and quadratic or "nearly" quadratic, the local solution is unique. Yet, in nonconvex case (as also here), local solutions are rather a general and rather broad framework. Various refined concepts have been devised, ranging from energetic solutions (which conserves energy) to approximable, vanishing-viscosity, BV-, or maximally-dissipative solutions, cf. in particular [35, 43] and also [15, 33] for a survey of even more concepts and a comparison. In our adhesive-contact context, there are essentially two extreme cases to be considered which, roughly speaking, delaminate either as early or as late as possible, being governed either by energy or by stress, and being approximable either by fully implicit or by a specific semi-implicit time discretizations, respectively.

The former, *energetic solution* (ES) concept requires, in addition to (24), also the full *stability*:

$$\forall\,(\tilde{\mathbf{u}},\tilde\zeta,\tilde\pi):\quad\mathcal{E}(t,\mathbf{u}(t),\zeta(t),\pi(t))\le\mathcal{E}(t,\tilde{\mathbf{u}},\tilde\zeta,\tilde\pi)+\mathcal{R}(\tilde\zeta-\zeta(t),\tilde\pi-\pi(t))\tag{25}$$

to be valid for a.a. t. Then, in fact, (25) is valid for all t and (24a) holds as an equality; for quite technical analytical details behind this highly nontrivial fact we

refer to [15, Sect. 7] or [33, Prop.3.11], or also [40, Prop. 5.4]. Such solutions conserve energy, being thus called *energetic solutions* (ES), invented in [35]. Note also that (25) obviously implies both (24b) and (24c, 24d).

The latter, stress driven, maximally-dissipative local-solution (MDLS), concept can be selected by requiring, in addition to (24), Hill's [23] *maximum-dissipation principle*, known also as an orthogonality principle [64], expressing that (3b) is equivalent to $\langle \widetilde{f} - f, v - \dot\zeta\rangle \geq 0$ for any v and any $\widetilde{f} \in \partial_{\dot\zeta}\mathcal{R}(v)$ with the so-called available driving force $f \in -\partial_\zeta\mathcal{E}(t, \mathbf{u}, \zeta, \pi)$; the adjective "available" becomes sensible especially if $\partial_\zeta\mathcal{E}(t, \mathbf{u}, \zeta, \pi)$ is set-valued because not all available f's are compatible with $f \in \partial_{\dot\zeta}\mathcal{R}(\dot\zeta)$ and can be realized during evolution. In particular, for $v = 0$, using also 1-homogeneity of $\mathcal{R}$, we obtain the announced principle which can, very formally, be written as

$$\langle f, \dot\zeta\rangle = \max_{f\in\partial_{\dot\zeta}\mathcal{R}(0)} \langle \widetilde{f}, \dot\zeta\rangle \text{ with } f \in -\partial_\zeta\mathcal{E}(t,\mathbf{u},\zeta,\pi), \tag{26a}$$

and similarly from (3c) we obtain

$$\langle g, \dot\pi\rangle = \max_{g\in\partial_{\dot\pi}\mathcal{R}(0)} \langle \widetilde{g}, \dot\pi\rangle \text{ with } g \in -\partial_\pi\mathcal{E}(t,\mathbf{u},\zeta,\pi). \tag{26b}$$

Note that the "max" terms are exactly $\mathcal{R}(\dot\zeta,0)$ and $\mathcal{R}(0,\dot\pi)$, respectively. Let us emphasize that, in general, $\dot\zeta$ and $\dot\pi$ are measures possibly having singular parts concentrated at rupture times where the solution and also the driving forces need not be continuous, so that the dualities in (26) are not well defined. For this reason, an *Integrated* version of the *Maximum-Dissipation Principle* (IMDP) was devised in [43], which reads here as:

$$\int_{t_1}^{t_2} f(t)\,\mathrm{d}\zeta(t) = \int_{t_1}^{t_2} \mathcal{R}(\dot\zeta,0)\mathrm{d}t \,(=\mathrm{Diss}_{\mathcal{R}}(\zeta,0;[t_1,t_2]))$$
$$\text{with some } f(t) \in -\partial_\zeta\mathcal{E}(t,\mathbf{u},\zeta,\pi), \tag{27a}$$

$$\int_{t_1}^{t_2} g(t)\,\mathrm{d}\pi(t) = \int_{t_1}^{t_2} \mathcal{R}(0,\dot\pi)\mathrm{d}t \,(=\mathrm{Diss}_{\mathcal{R}}(0,\pi;[t_1,t_2]))$$
$$\text{with some } g(t) \in -\partial_\pi\mathcal{E}(t,\mathbf{u},\zeta,\pi) \tag{27b}$$

to be valid for any $0 \leq t_1 < t_2 \leq T$. This definition is inevitably a bit technical and, without sliding into too much details, let us only mention that the first integrals in (27) are so-called lower Riemann-Stieltjes integrals defined by suprema of lower Darboux sums, i.e. in the case (27a) the left-hand-side integral is defined as $\int_r^s f(t)\,\mathrm{d}\zeta(t) := \sup_{N\in\mathbb{N},\ r=t_0<t_1<\ldots<t_{N-1}<t_N=s} \sum_{j=1}^{N} \inf_{t\in[t_{j-1},t_j]} \langle f(t), \zeta(t_j) - \zeta(t_{j-1})\rangle$ while the right-hand side integral is just an integral of a measure and its specific value is just the Diss-term as defined in (24a).

The IMDP (27) is satisfied on any interval $[t_1, t_2]$ where the solution is absolutely continuous; then the integrals in (27) are the conventional Lebesgue integrals. Thus the particular importance of IMDP is at jumps, i.e. at times when abrupt delamination possibly happens.

It is shown in [34, 43] on various finite-dimensional examples of "damageable springs" that this IMDP can identify too early rupturing local solutions (in particular the energetic ones) and its satisfaction for left-continuous local solutions indicates that the evolution is stress driven. On the other hand, it does not need to be satisfied even in physically well justified stress-driven local solutions. E.g. it happen if two springs with different fracture toughness organized in parallel rupture at the same time (but even in this situation our algorithm from Sect. 3.2 gives a correct approximate solution). Existence of left-continuous local solutions complying with IMDP has not been proved in general, yet. Therefore, we will rely rather on some approximation of IMDP, as described further in Sect. 3.2.

3 Computer implementation

For computer implementation, we are first to perform time and then spatial discretization. The time-discretization uses the fully implicit formula for ES combined with global minimization and a suitable semi-implicit formula for MDLS, both with an equidistant partition of the time interval $[0, T]$ by a time step τ, assuming T/τ integer. Actually, these two options seem to be the only ones which yield a discrete analogy of the upper energy inequality (24a) for $t_1 = 0$, cf. (29) below summed for $k = 1, \ldots$, and thus also basic a-priori estimates guaranteeing numerical stability and, at the end, also convergence for $\tau \to 0$, cf. [43, 44]. For example, the fully-implicit formula combined with local minimization (often used in engineering calculations) does not seem to guarantee it.

Actually, as we consider purely quasistatic problem without any inertial effects, there is algorithmically well possible to vary the time step τ within time levels. Also all mentioned theoretical estimates are kept and, if the maximal time step is made converging to zero, also the convergence is preserved. One can apply various adaptive strategies based either on controlling accuracy in energetics or, in case of MDLS, in approximate maximum-dissipation principle. Yet, it is not the focus of this paper and, as already said, we will consider only equidistant partitions of $[0,T]$.

As long as the material is linear and isotropic and our quasistatic isothermal problem can be formulated in terms of the boundary data only, see (1) and (2), the spatial discretization can advantageously be performed by a BEM. The present standard approximation of the distributions for $\mathbf{u}$, ζ, and π uses continuous linear boundary elements [39].

3.1 Discretization in time by the fully implicit formula

To satisfy the energy balance (24a) and the stability condition (25) also after discretization, the minimization problem for the solution at the successive step k is solved, once the solution for the time step $k-1$ is known and, in case of non-uniqueness, chosen, cf. [25]. More specifically, this problem is:

$$\begin{aligned}&\text{minimize}\quad \mathcal{H}^{\mathrm{k}}(\mathbf{u},\zeta,\pi)=\mathcal{E}(\mathrm{k}\tau,\mathbf{u},\zeta,\pi)\\&\quad+\mathcal{R}(\zeta-\zeta^{k-1},\pi-\pi^{k-1}).\end{aligned}\tag{28}$$

This recursive time-stepping procedure starts from the solution at $k=1$ calculated by using the initial conditions (24e).

Due to the character of the present delamination problem model (allowing sudden ruptures), the functional $\mathcal{H}^k$ is inevitably nonconvex. This nonconvexity requires applying a special numerical treatment in the minimization algorithm. The AMA proposed in the context of fracture mechanics in [9], and used also in [38, 44, 47], has been used to split the minimization to alternation between minimization with respect to $(\mathbf{u},\pi)$ and with respect to ζ, each of these being a minimization of a convex functional. Such alternation, however, does not have to lead to global minimization which is a characteristic feature behind ES, as pointed out already in [10]. Therefore a *back-tracking algorithm* (BTA) to control such a process has been utilized, providing that the energy (im)balance (24a) as an equality, in discrete form converted to a two-sided inequality, is satisfied, see [5, 38, 44, 47]. This *two-sided energy inequality* can be written in the following form, relying on the minimization of $\mathcal{H}^k$ in two subsequent time steps:

$$\begin{aligned}&\int_{(k-1)\tau}^{k\tau}\frac{\partial}{\partial t}\mathcal{E}(t,\mathbf{u}^k,\zeta^k,\pi^k)\mathrm{d}t\le\mathcal{E}(k\tau,\mathbf{u}^k,\zeta^k,\pi^k)\\&\quad-\mathcal{E}((k-1)\tau,\mathbf{u}^{k-1},\zeta^{k-1},\pi^{k-1})\\&\quad+\mathcal{R}(\zeta^k-\zeta^{k-1},\pi^k-\pi^{k-1})\\&\quad\le\int_{(k-1)\tau}^{k\tau}\frac{\partial}{\partial t}\mathcal{E}(t,\mathbf{u}^{k-1},\zeta^{k-1},\pi^{k-1})\mathrm{d}t.\end{aligned}\tag{29}$$

In fact, $(\mathbf{u}^k,\zeta^k,\pi^k)$ is the minimizer of $\mathcal{H}^k$, which means, by the degree-1 homogeneity of $\mathcal{R}$ for any $(\tilde{\mathbf{u}},\tilde{\zeta},\tilde{\pi})$ that

$$\begin{aligned}&\mathcal{E}(k\tau,\mathbf{u}^k,\zeta^k,\pi^k)\le\mathcal{E}(k\tau,\tilde{\mathbf{u}},\tilde{\zeta},\tilde{\pi})+\mathcal{R}(\tilde{\zeta}-\zeta^{k-1},\tilde{\pi}\\&\quad-\pi^{k-1})-\mathcal{R}(\zeta^k-\zeta^{k-1},\pi^k-\pi^{k-1})\le\mathcal{E}(k\tau,\tilde{\mathbf{u}},\tilde{\zeta},\tilde{\pi})\\&\quad+\mathcal{R}(\tilde{\zeta}-\zeta^k,\tilde{\pi}-\pi^k),\end{aligned}\tag{30}$$

which is the discrete analogy of the full stability (25), and, in particular, also

$$\begin{aligned}&\mathcal{E}(k\tau,\mathbf{u}^k,\zeta^k,\pi^k)+\mathcal{R}(\zeta^k-\zeta^{k-1},\pi^k-\pi^{k-1})\\&\quad\le\mathcal{E}(k\tau,\mathbf{u}^{k-1},\zeta^{k-1},\pi^{k-1}).\end{aligned}\tag{31}$$

Subtracting the term $\mathcal{E}((k-1)\tau,\mathbf{u}^{k-1},\zeta^{k-1},\pi^{k-1})$ from both sides of (31), we obtain, after a little calculus, the upper estimate in (29). Writing (30) at the level $k-1$ and testing it by $(\tilde{\mathbf{u}},\tilde{\zeta},\tilde{\pi})=(\mathbf{u}^k,\zeta^k,\pi^k)$ yields

$$\begin{aligned}&\mathcal{E}((k-1)\tau,\mathbf{u}^{k-1},\zeta^{k-1},\pi^{k-1})\le\mathcal{E}((k-1)\tau,\mathbf{u}^k,\zeta^k,\pi^k)\\&\quad+\mathcal{R}(\zeta^k-\zeta^{k-1},\pi^k-\pi^{k-1}),\end{aligned}\tag{32}$$

and adding the term $\mathcal{E}(k\tau,\mathbf{u}^k,\zeta^k,\pi^k)$ to both sides of (32), we obtain the lower estimate in (29). The upper estimate in (29) serves for a-priori estimates and thus numerical stability of the proposed scheme and further also for the convergence for $\tau\to 0$ and $h\to 0$ with a spatial-mesh parameter h introduced in Sect. 3.3.

The scheme of AMA follows (the superscript index in parentheses is used to denote the iterations within AMA, while without parentheses it is the time step):

1. For next $k = 1, 2, \ldots, T/\tau$ set $j = 0$, $\mathbf{u}^{(0)} = \mathbf{u}^{k-1}$, $\pi^{(0)} = \pi^{k-1}$ and $\zeta^{(0)} = \zeta^{k-1}$.
2. While $\|\zeta^{(j)} - \zeta^{(j-1)}\| \geq \varepsilon$, do:
   (a) Set next j.
   (b) Solve for $\mathbf{u}^{(j)} = \mathbf{u}$ and $\pi^{(j)} = \pi$: the minimization problem of $\mathcal{H}^k(\mathbf{u}, \zeta^{(j-1)}, \pi)$ subjected to boundary conditions.
   (c) Solve for $\zeta^{(j)} = \zeta$: the minimization problem of $\mathcal{H}^k(\mathbf{u}^{(j)}, \zeta, \pi^{(j)})$ subjected to the condition $0 \leq \zeta \leq \zeta^{k-1}$.
3. Put $\mathbf{u}^k = \mathbf{u}^{(j)}$, $\pi^k = \pi^{(j)}$ and $\zeta^k = \zeta^{(j)}$.

The proposed energy-based BTA obeys the following scheme:

1. Initiation: $k = 1$, $\zeta^{(0)} = 1$.
2. While $k \leq T/\tau$ do:
   (a) Use AMA to find ζ^k from the initial value $\zeta^{(0)}$.
   (b) Set $\zeta^{(0)} = \zeta^k$.
   (c) Check the discrete two-sided energy condition (29): if satisfied, increase k by one, otherwise decrease k by one (this is the actual back-tracking).

The goal of the step (c) is to start the iterations of AMA with some different initial iteration if the one from the previous time step was obviously not successful from the viewpoint of (29) which should ultimately be satisfied. Not to try randomly chosen starting iteration, the idea is to use some states from previous unsuccessful trials for larger values of k.

Although there is no guaranty that this iterative process converges to the global minimum, the practical experience with this energy-based BTA, however, shows that it provides a solution with lower energy than that obtained by mere AMA [5, 38, 44, 47] and often leads to satisfaction of (29) under given loading regimes. Yet, it should be emphasized that, although based on the assumption of global minimization, the satisfaction of the two-sided energy estimate (29), which this BTA tries to achieve, itself does not imply that the obtained solutions are global minimizers of the incremental problem (28). It only underlines algorithmic difficulties related to ES and, besides physical arguments, advocates advantages of the MDLS strategy.

Let us also note that an alternative variant of BTA has been proposed in [8, Sect. 2.4] and used also in [10], based on special properties of the particular problem studied therein, namely 2-homogeneity of the stored energy and monotonically increasing load. As a matter of fact, there is no universal hint for solving nonconvex global-minimization problems and other global-minimization strategies are to be thought about too, e.g. the so-called simulated annealing, etc.

3.2 Discretization in time by a semi-implicit formula

For finding the MDLS, we use a fractional-step-type semi-implicit time discretization devised in [45], see also [48], such that the problem is split into two convex minimizations similarly as done in AMA above, yet it must be emphasized that AMA is now used only in one iteration at each time level. Therefore, in contrast to ES strategy, there are no difficulties with global minimization and the numerical calculation is much easier with no need of repeating the minimization or backtracking, and additionally it prevents the solution from non-physically too early debonding or from sliding non-physically into the less dissipative Mode I, cf. also Fig. 10 below. More specifically, considering ζ^{k-1} and π^{k-1} known from the previous time step, the problem includes two subsequent minimizations. First,

$$\begin{aligned} &\text{minimize} \quad \mathcal{H}^k_\pi(\mathbf{u}, \pi) = \mathcal{E}(k\tau, \mathbf{u}, \zeta^{k-1}, \pi) \\ &+ \mathcal{R}(0, \pi - \pi^{k-1}), \end{aligned} \tag{33a}$$

and, denoting its unique minimizer $(\mathbf{u}^k, \pi^k)$, second

$$\begin{aligned} &\text{minimize} \\ &\mathcal{H}^k_\zeta(\zeta) = \mathcal{E}(k\tau, \mathbf{u}^k, \zeta, \pi^k) + \mathcal{R}(\zeta - \zeta^{k-1}, 0), \end{aligned} \tag{33b}$$

with the minimizer ζ^k. Again, this recursive time-stepping procedure naturally starts from the solution at $k = 1$ calculated by using the initial conditions (24e).

To see that the system (33) guarantees a discrete analogy of the conditions for local solutions (24), we can proceed as explained in the following. First, as ζ^k is the minimizer of $\mathcal{H}^k_\zeta$ and $\mathcal{R}(\cdot, 0)$ is homogeneous of degree 1, we have for any $\tilde{\zeta}$, like in (30), that $\mathcal{E}(k\tau, \mathbf{u}^k, \zeta^k, \pi^k) \leq \mathcal{E}(k\tau, \mathbf{u}^k, \tilde{\zeta}, \pi^k) + \mathcal{R}(\tilde{\zeta} - \zeta^k, 0)$, which provides a discrete analogy of (24c). Second, as

$(\mathbf{u}^k,\pi^k)$ is the minimizer of $\mathcal{H}^k_\pi$ and $\mathcal{R}(0,\cdot)$ is homogeneous of degree 1, we have for any $(\tilde{\mathbf{u}},\tilde{\pi})$ that

$$\mathcal{E}(k\tau,\mathbf{u}^k,\zeta^{k-1},\pi^k)\le\mathcal{E}(k\tau,\tilde{\mathbf{u}},\zeta^{k-1},\tilde{\pi})+\mathcal{R}(0,\tilde{\pi}-\pi^k), \tag{34}$$

which provides a discrete analogy of both (24b) and (24d). These minimization properties of ζ^k and of $(\mathbf{u}^k,\pi^k)$ also allow us to write

$$\begin{aligned}&\mathcal{E}(k\tau,\mathbf{u}^k,\zeta^{k-1},\pi^k)+\mathcal{R}(0,\pi^k-\pi^{k-1})\\&\quad\le\mathcal{E}(k\tau,\mathbf{u}^{k-1},\zeta^{k-1},\pi^{k-1})\end{aligned} \tag{35a}$$

and

$$\begin{aligned}&\mathcal{E}(k\tau,\mathbf{u}^k,\zeta^k,\pi^k)+\mathcal{R}(\zeta^k-\zeta^{k-1},0)\\&\quad\le\mathcal{E}(k\tau,\mathbf{u}^k,\zeta^{k-1},\pi^k),\end{aligned} \tag{35b}$$

which after summation cancels the terms $\mathcal{E}(k\tau,\mathbf{u}^k,\zeta^{k-1},\pi^k)$ and gives again (31), and then further the upper estimate in (29) which is a discrete analogy of (24a). The minimization of (33) thus provide an approximation of all conditions defining local solution, cf. (24).

Denoting the left-continuous piecewise-constant interpolants $(u_\tau,\zeta_\tau,\pi_\tau)$ of the values $(u^k_\tau,\zeta^k_\tau,\pi^k_\tau)$, i.e. $u_\tau(k\tau)=u^k_\tau$ etc., one can devise the discrete analogy of the integrated maximum-dissipation principle (27) straightforwardly for these left-continuous interpolants, required however to hold only asymptotically. More specifically, in analogy to (27) formulated equivalently for all $[0,t]$ instead of $[t_1,t_2]$, one can expect an *Approximate Maximum-Dissipation Principle* (AMDP) in the form

$$\begin{aligned}&\int_0^t f_\tau\,\mathrm{d}\zeta_\tau\ \overset{?}{\sim}\ \mathrm{Diss}_{\mathcal{R}}(\zeta_\tau,0;[0,t])\ \text{for some}\\&f_\tau(t)\in-\partial_\zeta\bar{\mathcal{E}}_\tau(t,\mathbf{u}_\tau(t),\zeta_\tau(t-\tau),\pi_\tau(t)),\end{aligned} \tag{36a}$$

$$\begin{aligned}&\int_0^t g_\tau\,\mathrm{d}\pi_\tau\ \overset{?}{\sim}\ \mathrm{Diss}_{\mathcal{R}}(0,\pi_\tau;[0,t])\ \text{ for some}\\&g_\tau(t)\in-\partial_\pi\bar{\mathcal{E}}_\tau(t,\mathbf{u}_\tau(t),\zeta_\tau(t),\pi_\tau(t)),\end{aligned} \tag{36b}$$

where again the integrals are the lower Riemann-Stieltjes integrals as in (27) and where $\bar{\mathcal{E}}_\tau(\cdot,\mathbf{u},\zeta,\pi)$ is the left-continuous piecewise-constant interpolant of the values $\mathcal{E}(k\tau,\mathbf{u},\zeta,\pi),k=0,1,\ldots,T/\tau$. Moreover, "$\overset{?}{\sim}$" in (36) means that the equality holds possibly only asymptotically for $\tau\to0$ but even this is rather only desirable and not always valid. Anyhow, loadings which, under given geometry of the specimen, lead to rate-independent slides where the solution is absolutely continuous will always comply with AMDP (36). Also, some finite-dimensional examples of "damageable springs" in [34, 43] show that this AMDP can detect too early rupturing local solutions (in particular the energetic ones) while it generically holds for solutions obtained by the semi-implicit algorithm (33).

Now, for the piecewise-constant interpolants, we can simply evaluate the integrals explicitly, so that AMDP (36) reads

$$\begin{aligned}\Delta R_{\zeta,\tau}(t):=&\int_{\Gamma_{\mathrm{C}}}G_{\mathrm{d}}\big(\zeta^K_\tau-\zeta_0\big)\,\mathrm{d}S\\&-\sum_{k=1}^K\int_{\Gamma_{\mathrm{C}}}f^{k-1}_\tau(\zeta^k_\tau-\zeta^{k-1}_\tau)\,\mathrm{d}S\ \overset{?}{\sim}0\end{aligned} \tag{37a}$$

and

$$\begin{aligned}\Delta R_{\pi,\tau}(t):=&\sum_{k=1}^K\int_{\Gamma_{\mathrm{C}}}\sigma_{\mathrm{yield}}\big|\pi^k_\tau-\pi^{k-1}_\tau\big|\,\mathrm{d}S\\&-\sum_{k=1}^K\int_{\Gamma_{\mathrm{C}}}g^{k-1}_\tau(\pi^k_\tau-\pi^{k-1}_\tau)\,\mathrm{d}S\overset{?}{\sim}0\\&\text{where } K=\max\{k\in\mathbb{N};\ k\tau\le t\}\text{ and}\\&\text{where } f^k_\tau\in-\partial_\zeta\mathcal{E}(u^k_\tau,\zeta^{k-1}_\tau,\pi^k_\tau)\text{ and}\\&g^k_\tau\in-\partial_\pi\mathcal{E}(u^k_\tau,\zeta^k_\tau,\pi^k_\tau).\end{aligned} \tag{37b}$$

Always, the left-hand sides in (36) are below the right-hand sides, and one can a-posteriori check the residua $\Delta R_{\zeta,\tau}\ge0$ and $\Delta R_{\pi,\tau}\ge0$ depending on t (or possibly also on space, as in Fig. 21 below). Even though IMDP (27) and similarly AMDP (36) do not need to hold even for physically relevant stress-driven local solutions (typically when several "springs" rupture at the same time, some of them being still at the sub-critical stress before the rupture), a good satisfaction of AMDP (36) can always be counted as valuable a-posteriori justification of the (otherwise not physically based) simple and numerically efficient fractional-step-type algorithm (33) and distribution of the residuum in (36) in time (or in space) can serve for some possible adaptive refinement strategies.

3.3 Spatial discretization and SGBEM

The role of the SGBEM [7, 49, 57] in the present computational procedure is to solve a BVP for each subdomain separately in order to calculate the elastic strain energy in these subdomains. Thus, at each time step and at each iteration of the minimization algorithm, the SGBEM code calculates unknown tractions along $\Gamma_C \cup \Gamma_u$, supposing the displacements at Γ_C to be known from the used minimization procedure, in a similar way as proposed and tested using a collocational BEM code in [38, 44, 45, 48].

The chosen Symmetric Galerkin BEM can be deduced from the potential energy principles [6, 7, 61, 62]. This fact guarantees the positive definite character of the strain energy computed by SGBEM, in contrast to the classical collocational BEM, see [53, 62] for details and further references. The *Boundary Integral Equation*s (BIE) solved by SGBEM are the Somigliana displacement and traction identities, written for each particular subdomain Ω^η separately:

$$\frac{1}{2}u_k^\eta(x) = \int_{\Gamma^\eta} U_{kl}^\eta(x,y)t_l^\eta(y)\mathrm{d}S(y) - \fint_{\Gamma^\eta} T_{kl}^\eta(x,y)u_l^\eta(y)\mathrm{d}S(y), \text{ for a.a. } x \in \Gamma_u^\eta \cup \Gamma_C, \tag{38a}$$

$$\frac{1}{2}t_k^\eta(x) = \fint_{\Gamma^\eta} T_{kl}^{\eta *}(x,y)t_l^\eta(y)\mathrm{d}S(y) - \fint_{\Gamma^\eta} S_{kl}^\eta(x,y)u_l^\eta(y)\mathrm{d}S(y), \text{ for a.a. } x \in \Gamma_t^\eta. \tag{38b}$$

The integral kernels in the above equations are given by the (weakly singular) Kelvin fundamental solution $U_{ij}^\eta(x,y)$—the response of the elastic plane to a point load, and the associated derivative kernels obtained by the differential traction operator applied with respect to one or both variables—the strongly singular kernels $T_{ij}^\eta(x,y)$ and $T_{ij}^{\eta *}(x,y)$ and the hypersingular kernel $S_{ij}^\eta(x,y)$. It should also be noted that the free-term coefficients $\frac{1}{2}$ are valid only at smooth boundary parts. Due to the integral kernel singularities, the integrals denoted by $\fint_\Gamma$ and $\fint_\Gamma$ stand for the Cauchy principal value and the Hadamard finite part of the integral, respectively.

As follows from the previous explanations, the SGBEM code is used merely to elastic strain energy computation in the bulk and does not include the solution of the whole interface problem, which is left to the suitable minimization algorithm, see also [38, 44, 45, 48].

Applying the standard SGBEM approach [61, 62] to (38) together with the boundary conditions from Sect. 2, we obtain the following equation:

$$\begin{aligned}
0 = \int_{\Gamma_u^\eta} \varphi_j^\eta(y) \Bigg(& - \int_{\Gamma_u^\eta} U_{ji}^\eta(y,x)t_i^\eta(x)\mathrm{d}_x S + \int_{\Gamma_t^\eta} T_{ji}^\eta(y,x)u_i^\eta(x)\mathrm{d}_x S - \int_{\Gamma_C} U_{ji}^\eta(y,x)t_i^\eta(x)\mathrm{d}_x S \\
& + \int_{\Gamma_C} T_{ji}^\eta(y,x)u_i^\eta(x)\mathrm{d}_x S + \Big(\frac{1}{2}w_j^\eta(y) + \fint_{\Gamma_u^\eta} T_{ji}^\eta(y,x)w_i^\eta(x)\mathrm{d}_x S\Big)\Bigg)\mathrm{d}_y S \\
& + \int_{\Gamma_t^\eta} \psi_j^\eta(y) \Bigg(\int_{\Gamma_u^\eta} T_{ji}^{\eta *}(y,x)t_i^\eta(x)\mathrm{d}_x S - \fint_{\Gamma_t^\eta} S_{ji}^\eta(y,x)u_i^\eta(x)\mathrm{d}_x S + \int_{\Gamma_C} T_{ji}^{\eta *}(y,x)t_i^\eta(x)\mathrm{d}_x S \\
& - \int_{\Gamma_C} S_{ji}^\eta(y,x)u_i^\eta(x)\mathrm{d}_x S - \int_{\Gamma_u^\eta} S_{ji}^\eta(y,x)w_i^\eta(x)\mathrm{d}_x S\Bigg)\mathrm{d}_y S \\
& + \int_{\Gamma_C} \varphi_j^\eta(y) \Bigg(- \int_{\Gamma_u^\eta} U_{ji}^\eta(y,x)t_i^\eta(x)\mathrm{d}_x S + \int_{\Gamma_t^\eta} T_{ji}^\eta(y,x)u_i^\eta(x)\mathrm{d}_x S - \int_{\Gamma_C} U_{ji}^\eta(y,x)t_i^\eta(x)\mathrm{d}_x S \\
& + \Big(\frac{1}{2}u_j^\eta(y) + \fint_{\Gamma_C} T_{ji}^\eta(y,x)u_i^\eta(x)\mathrm{d}_x S\Big) + \int_{\Gamma_u^\eta} T_{ji}^\eta(y,x)w_i^\eta(x)\mathrm{d}_x S\Bigg)\mathrm{d}_y S.
\end{aligned} \tag{39}$$

The weighted formulation of the BIE system (39) can be rewritten in a compact and transparent form by introducing the following operator notation:

$$\boldsymbol{\omega}_q^{\eta T}\mathbf{Z}_{qr}^{\eta}\mathbf{v}_r^{\eta} = \int_{\Gamma_q^{\eta}} \omega_j^{\eta}(y)\left(\int_{\Gamma_r^{\eta}} Z_{ji}^{\eta}(y,x)v_i^{\eta}(x)\mathrm{d}_x S\right)\mathrm{d}_y S, \tag{40}$$

where ω stands for φ or ψ; v stands for u or t, q and r stand for u, t or c; and Z stands for U, T, T^* or S; and where the inner integral can be regular, weakly singular, Cauchy principal value or Hadamard finite part integral. Then, (39) reads

$$\begin{aligned} 0 = \boldsymbol{\varphi}_u^{\eta\,T}\Big(& -\mathbf{U}_{uu}^{\eta}\mathbf{t}_u^{\eta} + \mathbf{T}_{ut}^{\eta}\mathbf{u}_t^{\eta} - \mathbf{U}_{uc}^{\eta}\mathbf{t}_c^{\eta} + \mathbf{T}_{uc}^{\eta}\mathbf{u}_c^{\eta} \\ & + \left(\frac{1}{2}\mathbf{I}_{uu}^{\eta} + \mathbf{T}_{uu}^{\eta}\right)\mathbf{w}^{\eta}\Big) \\ & + \boldsymbol{\psi}_t^{\eta\,T}\left(\mathbf{T}_{tu}^{\eta *}\mathbf{t}_u^{\eta} - \mathbf{S}_{tt}^{\eta}\mathbf{u}_t^{\eta} + \mathbf{T}_{tc}^{\eta *}\mathbf{t}_c^{\eta} - \mathbf{S}_{tc}^{\eta}\mathbf{u}_c^{\eta} - \mathbf{S}_{uu}^{\eta}\mathbf{w}^{\eta}\right) \\ & + \boldsymbol{\varphi}_c^{\eta\,T}\Big(- \mathbf{U}_{cu}^{\eta}\mathbf{t}_u^{\eta} + \mathbf{T}_{ct}^{\eta}\mathbf{u}_t^{\eta} - \mathbf{U}_{cc}^{\eta}\mathbf{t}_c^{\eta} \\ & + \left(\frac{1}{2}\mathbf{I}_{cc}^{\eta} + \mathbf{T}_{cc}^{\eta}\right)\mathbf{u}_c^{\eta} + \mathbf{T}_{cu}^{\eta}\mathbf{w}^{\eta}\Big), \end{aligned} \tag{41}$$

or equivalently in a matrix-operator form

$$\begin{aligned} & \begin{pmatrix} \boldsymbol{\varphi}_u^{\eta} \\ \boldsymbol{\psi}_t^{\eta} \\ \boldsymbol{\varphi}_c^{\eta} \end{pmatrix}^{\top} \begin{pmatrix} -\mathbf{U}_{uu}^{\eta} & \mathbf{T}_{ut}^{\eta} & -\mathbf{U}_{uc}^{\eta} \\ \mathbf{T}_{tu}^{\eta *} & -\mathbf{S}_{tt}^{\eta} & \mathbf{T}_{tc}^{\eta *} \\ -\mathbf{U}_{cu}^{\eta} & \mathbf{T}_{ct}^{\eta} & -\mathbf{U}_{cc}^{\eta} \end{pmatrix} \begin{pmatrix} \mathbf{t}_u^{\eta} \\ \mathbf{u}_t^{\eta} \\ \mathbf{t}_c^{\eta} \end{pmatrix} \\ & = \begin{pmatrix} \boldsymbol{\varphi}_u^{\eta} \\ \boldsymbol{\psi}_t^{\eta} \\ \boldsymbol{\varphi}_c^{\eta} \end{pmatrix}^{\top} \begin{pmatrix} -\frac{1}{2}\mathbf{I}_{uu}^{\eta} - \mathbf{T}_{uu}^{\eta} & -\mathbf{T}_{uc}^{\eta} \\ \mathbf{S}_{uu}^{\eta} & \mathbf{S}_{tc}^{\eta} \\ -\mathbf{T}_{cu}^{\eta} & -\frac{1}{2}\mathbf{I}_{cc}^{\eta} - \mathbf{T}_{cc}^{\eta} \end{pmatrix} \begin{pmatrix} \mathbf{w}^{\eta} \\ \mathbf{u}_c^{\eta} \end{pmatrix}. \end{aligned} \tag{42}$$

In the previous relations, $\mathbf{I}^{\eta}$ denotes the identity operator with the subscripts specifying the part of the boundary where it is restricted. The functions $\boldsymbol{\varphi}^{\eta}$ and $\boldsymbol{\psi}^{\eta}$ represent the virtual tractions and displacements respectively, and the system in (42) has to be satisfied for any virtual functions.

The symmetric BIE system (42) will be solved numerically by SGBEM. To this end, each boundary Γ^{η} is discretized by a boundary element mesh with the maximum size of the elements denoted by h. Then, the functions defined on Γ^{η} are approximated by continuous linear boundary elements [39] allowing discontinuities of tractions at the element junctions if required. Thus, the approximation formulas can be written in the form

$$\mathbf{u}^{\eta}(x) = \sum_p \mathbf{N}_{\psi p}^{\eta}(x)\mathsf{u}_p^{\eta}, \quad \mathbf{t}^{\eta}(x) = \sum_l \mathbf{N}_{\varphi l}^{\eta}(x)\mathsf{t}_l^{\eta}, \tag{43}$$

where $\mathbf{N}_{\psi p}^{\eta}(x)$ and $\mathbf{N}_{\varphi p}^{\eta}(x)$, respectively, are matrices containing the shape functions of displacements and tractions associated to node p at $x_p^{\eta} \in \Gamma^{\eta}$, and u_p^{η} and t_p^{η}, respectively, are vectors containing the components of the displacement and traction vector at the node p. Let u^{η}, w^{η}, and t^{η}, respectively, denote the vectors containing all unknown nodal displacements, all prescribed nodal displacements, and all unknown nodal tractions associated to Γ^{η}. Let the subvectors of the nodal unknowns at the boundary parts Γ_u^{η}, Γ_t^{η} and Γ_{C}, respectively, be distinguished by the same subscripts u, t, and c. The set of vectors of virtual functions $\boldsymbol{\psi}^{\eta}$ and $\boldsymbol{\varphi}^{\eta}$ can be chosen to be equal to shape functions associated to each nodal unknown and extended by zero to the whole boundary. Such a choice leads to the symmetric square matrix of the following system of linear algebraic equations:

$$\begin{aligned} & \begin{pmatrix} -\mathsf{U}_{uu}^{\eta} & \mathsf{T}_{ut}^{\eta} & -\mathsf{U}_{uc}^{\eta} \\ \mathsf{T}_{tu}^{\eta T} & -\mathsf{S}_{tt}^{\eta} & \mathsf{T}_{tc}^{\eta T} \\ -\mathsf{U}_{cu}^{\eta} & \mathsf{T}_{ct}^{\eta} & -\mathsf{U}_{cc}^{\eta} \end{pmatrix} \begin{pmatrix} \mathsf{t}_u^{\eta} \\ \mathsf{u}_t^{\eta} \\ \mathsf{t}_c^{\eta} \end{pmatrix} \\ & = \begin{pmatrix} -\frac{1}{2}\mathsf{M}_{uu}^{\eta} - \mathsf{T}_{uu}^{\eta} & -\mathsf{T}_{uc}^{\eta} \\ \mathsf{S}_{uu}^{\eta} & \mathsf{S}_{tc}^{\eta} \\ -\mathsf{T}_{cu}^{\eta} & -\frac{1}{2}\mathsf{M}_{cc}^{\eta} - \mathsf{T}_{cc}^{\eta} \end{pmatrix} \begin{pmatrix} \mathsf{w}^{\eta} \\ \mathsf{u}_c^{\eta} \end{pmatrix}. \end{aligned} \tag{44}$$

The elements of the submatrices denoted with letters U, T and S are formed by double integrals including the integral kernel denoted by the same letter as is usual in SGBEM. The square 2×2 submatrices, associated to nodes p and l, of the mass matrices M_{rr}^{η}, with r being u or c, are formed by the integrals:

$$\begin{aligned} (\mathsf{M}_{uu}^{\eta})_{lp} &= \int_{\Gamma_u^{\eta}} \mathbf{N}_{\varphi l}^{\eta\top}(x)\mathbf{N}_{\psi p}^{\eta}(x)\mathrm{d}_x S, \\ (\mathsf{M}_{cc}^{\eta})_{lp} &= \int_{\Gamma_{\mathrm{C}}} \mathbf{N}_{\varphi l}^{\eta\top}(x)\mathbf{N}_{\psi p}^{\eta}(x)\mathrm{d}_x S. \end{aligned} \tag{45}$$

3.4 Minimization algorithm

Once all the boundary data (displacements and tractions) are obtained from the solution of (44) for each subdomain, the energies $\mathcal{H}^k$ from (28) or $\mathcal{H}_{\pi}^k$ and $\mathcal{H}_{\zeta}^k$ from (33) can be calculated. It is worth seeing how

to calculate these energies for a given discretization. For the sake of brevity, it will be shown for the case of $\mathcal{H}^k$ only, whereas $\mathcal{H}^k_\pi$ and $\mathcal{H}^k_\zeta$ are evaluated similarly.

Prior to the calculation, let us reconsider the nonsmooth terms in $\mathcal{R}(\zeta-\zeta^{k-1},\pi-\pi^{k-1})$, cf. (2). The first one with ζ does not cause any problem because ζ must be non-increasing $\zeta^{k-1}\geq\zeta$ according to (2), thus $|\zeta-\zeta^{k-1}|=\zeta^{k-1}-\zeta$. For the second term, a classical trick of removing the absolute values and replacing them by additional unknowns with restrictions is used [4], relying on a polyhedral epigraph of this term obtained after discretization in the present 2D case. The solution of the original problem with $\mathcal{R}$ is equivalent to the solution with the following functional $\widetilde{\mathcal{R}}$:

$$\widetilde{\mathcal{R}}(\zeta-\zeta^{k-1},\mu)=\int_{\Gamma_C}\big(G_d\big(\zeta^{k-1}-\zeta\big)+\mu\big)\mathrm{d}S \tag{46a}$$

and the following unilateral affine constraints

$$0\leq\zeta\leq\zeta^{k-1}, \tag{46b}$$

$$\mu-\sigma_{\text{yield}}\pi\geq-\sigma_{\text{yield}}\pi^{k-1}, \tag{46c}$$

$$\mu+\sigma_{\text{yield}}\pi\geq\sigma_{\text{yield}}\pi^{k-1}. \tag{46d}$$

In the present disretization, the approximation formulas for the damage parameter ζ, plastic slip π and auxiliary parameter μ given by the pertinent boundary-element mesh are considered; it is worth noting that using piecewise constant boundary elements for plasticity variables leads directly to element-wise decoupling of (46c) and (46d). The approximation formulas can be written in the form

$$\begin{aligned}\zeta(x)&=\sum_m N_{\zeta m}(x)\zeta_m,\quad \pi(x)=\sum_m N_{\pi m}(x)\pi_m,\\ \mu(x)&=\sum_m N_{\mu m}(x)\mu_m,\end{aligned} \tag{47}$$

where $N_{\zeta m}(x), N_{\pi m}(x), N_{\mu m}(x)$, respectively, are shape functions of the damage, plastic slip, and auxiliary parameters associated to the node m, while ζ_m,π_m,μ_m are the pertinent nodal unknowns.

The energy $\mathcal{H}^k$, from the problem (28) defined by (1) and (46) and discretized by (43) and (47) then reads

$$\begin{aligned}\mathcal{H}^k(\mathbf{u},\zeta,\pi)=&\int_{\Gamma^A}\frac{1}{2}\sum_p \mathbf{N}^A_{\psi p}(x)\mathsf{u}^A_p\cdot\sum_l\mathbf{N}^A(x)\mathsf{t}^A_l\,\mathrm{d}S+\int_{\Gamma^B}\frac{1}{2}\sum_q\mathbf{N}_{\psi q}(x)\mathsf{u}^B_q\cdot\sum_r\mathbf{N}^B(x)\mathsf{t}^B_r\,\mathrm{d}S\\ &+\int_{\Gamma_C}\Bigg\{\sum_m N_{\zeta m}(x)\zeta_m\Bigg[\frac{1}{2}k_{\mathbf{n}}\Big(\sum_q N^B_{\psi nq}(x)u^B_{nq}-\sum_p N^A_{\psi np}(x)u_{np}\Big)^2\\ &+\frac{1}{2}k_{\mathbf{s}}\Big(\sum_q N^B_{\psi sq}(x)u^B_{sq}-\sum_p N^A_p(x)u^A_{sp}-\sum_m N_{\pi m}(x)\pi_m\Big)^2\Bigg]+\frac{1}{2}k_H\Big(\sum_m N_{\pi m}(x)\pi_m\Big)^2\Bigg\}\mathrm{d}S\\ &+\int_{\Gamma_C}\Bigg\{\frac{1}{2}k_0\Big[\sum_m(\nabla_{\mathbf{s}}N(x))\zeta_m\Big]^2+\frac{1}{2}k_1\Big[\sum_m(\nabla_{\mathbf{s}}N_{\pi m}(x))\pi_m\Big]^2\Bigg\}\mathrm{d}S\\ &+\int_{\Gamma_C}\Bigg[G\Big(\sum_m N_{\zeta m}(x)\big(\zeta^{k-1}_m-\zeta_m\big)\Big)+\sum_m N_{\mu m}(x)\mu_m\Bigg]\mathrm{d}S\end{aligned} \tag{48}$$

with the constraints

$$\sum_q N^{AB}_{npq}u^B_{nq}-u^A_{np}\geq 0\quad\text{for all pertinent } p, \tag{49a}$$

$$0\leq\zeta_m\leq\zeta^{k-1}_m\quad\text{for all pertinent } m, \tag{49b}$$

$$\mu_m-\sigma_{\text{yield}}\pi_m\geq-\sigma_{\text{yield}}\pi^{k-1}_m\quad\text{for all pertinent m}, \tag{49c}$$

$$\mu_m+\sigma_{\text{yield}}\pi_m\geq\sigma_{\text{yield}}\pi^{k-1}_m\quad\text{for all pertinent } m, \tag{49d}$$

where $N^{AB}_{npq}=N^B_{\psi nq}(x^A_p)$. In (48), $N^\eta_{\psi sp}$ and $N^\eta_{\psi np}$ are the shape functions like those in $N^\eta_{\psi p}$ approximating the normal and tangential displacements, respectively.

The minimization of the energy $\mathcal{H}^k$ is split into two parts, using AMA. The minimization procedure with respect to u and $\boldsymbol{\pi}$ (2b of AMA) can utilize any relevant quadratic programming approach with inequality constraints. Analogously, a similar minimization procedure with respect to $\boldsymbol{\zeta}$ can be applied

with a modification that the constraints are box type, see (49b).

It may be useful to reformulate the problem in such a way that the restrictions (49) change to bound constraints sometimes also called box constraints. The pair of constraints (49c) and (49d) for each node can be replaced using the following substitution for the nodal values

$$\begin{aligned} \omega_{1\,m} &= \mu_m - \sigma_{\text{yield}}\pi_m, \quad \omega_{1\,m} \geq 0, \\ \omega_{2\,m} &= \mu_m + \sigma_{\text{yield}}\pi_m, \quad \omega_{2\,m} \geq 0. \end{aligned} \tag{50}$$

The system (49a) provides l linearly independent constraints which can be written in a matrix form as

$$(\mathsf{N}_n^{\mathrm{AB}} - \mathsf{I}^{\mathrm{A}}) \begin{pmatrix} \mathsf{u}_n^{\mathrm{B}} \\ \mathsf{u}_n^{\mathrm{A}} \end{pmatrix} \geq \begin{pmatrix} \mathsf{0} \\ \mathsf{0} \end{pmatrix}, \tag{51}$$

with the identity matrix I^{A}. The inequality is defined by a full row-rank matrix. Thus, according to [17], introducing new variables y and z leads to

$$\begin{aligned} \begin{pmatrix} \mathsf{u}_n^{\mathrm{B}} \\ \mathsf{u}_n^{\mathrm{A}} \end{pmatrix} &= \begin{pmatrix} (\mathsf{N}_n^{\mathrm{AB}})^{\top} \\ -\mathsf{I}^{\mathrm{A}} \end{pmatrix} \left(\mathsf{N}_n^{\mathrm{AB}} (\mathsf{N}_n^{\mathrm{AB}})^{\top} + \mathsf{I}^{\mathrm{A}} \right)^{-1} \mathsf{y} \\ &+ \begin{pmatrix} \mathsf{K}^{\mathrm{B}} \\ \mathsf{K}^{\mathrm{A}} \end{pmatrix} \mathsf{z}, \text{ with } \mathsf{y} \geq \mathsf{0}, \end{aligned} \tag{52}$$

where columns of each K^{η} span the null-space of $(\mathsf{N}_n^{\mathrm{AB}}, -\mathsf{I}^{\mathrm{A}})$. We have thus the same number of bound constraints as provided by more general restrictions (49a).

The discretized functional (48), with some of the variables fixed according to the current phase of AMA, can be expressed in a general matrix form as

$$\begin{aligned} \mathcal{H}^k(\mathsf{y}) &= \frac{1}{2}\mathsf{y}^{\top}\mathsf{A}\mathsf{y} - \mathsf{b}^{\top}\mathsf{y}, \\ -\infty \leq \mathsf{y}_{\text{low}} \leq \mathsf{y} \leq \mathsf{y}_{\text{up}} &\leq +\infty. \end{aligned} \tag{53}$$

The bounds y_{low} and y_{up} depend on the problem to be solved and, as indicated, some of them may be infinite, meant as no restriction being applied for the pertinent component of y. The constrained minimum is then denoted by y^k. The standard algorithms use the matrix A explicitly which however is not calculated in the present approach. Nevertheless, the terms which arise from the first two integrals in the right-hand side of (48) provide the energy and calculating their derivative with respect to the unknown u they provide a projected traction $\mathsf{M}^{\top}\mathsf{t}$ with M defined as in (45). This projected traction can naturally be calculated in the SGBEM algorithm, and in equation (53) is in fact represented by the product Ay without explicit knowledge of A. Thus, each time the CG algorithm requires a matrix-by-vector product a system from SGBEM is solved. The influence matrices of SGBEM, however, do not have to be calculated more then once in all the solution process, as they are the same for all iterations and all time steps, considering only small displacements.

Conjugate gradient (CG) based algorithms with bound constraints [17] are used in the minimization procedures. Let us summarize briefly the main aspects of such methods. They naturally require an initial estimate of y^k which can be chosen, e. g., from the previous time step. The gradient $\mathsf{g} = \mathsf{A}\mathsf{y} - \mathsf{b}$, or strictly speaking a projected gradient g^P, has to be calculated for this estimate and also during the minimization algorithm as its norm may be a measure of the accuracy of the pertinent iteration—the exact solution has vanishing projected gradient.

The projected gradient g^P is a part of the gradient enabling the functional $\mathcal{H}^k$ to be minimized with respect to the constraints along the opposite direction. This is important in the situations where the particular iteration solution satisfies some bound constraints as equalities. The pertinent coordinates of the iteration solution are called active.

The gradient g is composed of several parts. Working directly with the components of the gradient is an advantage of the bound constraints, unlike the more general restrictions which were avoided according to the aforementioned explanations. The first part of the gradient g is the free gradient g^F which is equal to the gradient g only for non-active components, the active components are equal to zero. The second one is the chopped gradient g^C which is equal to zero for non-active components. For the active components, it may also be equal to zero if the sign of the gradient component does not enable constrained minimization in the opposite direction, it means that for the lower bounds it is nonzero only for the negative active components of g, and for the upper bounds it is nonzero only for the positive active components of g. Projected gradient is then a sum of the free and chopped gradients: $\mathsf{g}^P = \mathsf{g}^F + \mathsf{g}^C$. The remaining possibly nonzero part of the gradient g is not required for the constrained minimization.

The used CG based algorithms generally obey the following scheme (CG iteration denoted by numbers in parentheses):

1. Initiation: j=1, choose $\mathbf{y}^{(j)}$, calculate $\mathbf{g}$ and its parts $\mathbf{g}^P$, $\mathbf{g}^F$ and $\mathbf{g}^C$, initiate minimization direction $\mathbf{p}$=$\mathbf{g}^P$.
2. While $\|\mathbf{g}^P\| \geq \varepsilon$ do:
   (a) According to the norms of $\mathbf{g}^F$ and $\mathbf{g}^C$ select minimization:
      i. Case: $\mathbf{g}^F$ is more significant – a try with a CG step: $\mathbf{y}^{(\mathrm{try})}$ minimizes $\mathcal{H}^k$ from $\mathbf{y}^{(j)}$ in the direction of $-\mathbf{p}$
         A. If $\mathbf{y}^{(\mathrm{try})}$ satisfies all the constraints – a standard CG step: $\mathbf{y}^{(j+1)}$=$\mathbf{y}^{(\mathrm{try})}$, calculate new minimization direction $\mathbf{p}$ from the CG algorithm.
         B. If $\mathbf{y}^{(\mathrm{try})}$ fails in some constraints – expand the active set: $\mathbf{y}^{(j+1)}$ is found from $\mathbf{y}^{(j)}$ in the direction of $-\mathbf{p}$ up to or down to the closest bound, re-initiate minimization direction $\mathbf{p}$=$\mathbf{g}^F$
      ii. Case: $\mathbf{g}^C$ is more significant – make free some active components $\mathbf{y}^{(j+1)}$ minimizes $\mathcal{H}^k$ from $\mathbf{y}^{(j)}$ in the direction of $-\mathbf{g}^C$, re-initiate minimization direction $\mathbf{p}$=$\mathbf{g}^F$.
   (b) j=j+1.
3. $\mathbf{y}^k$=$\mathbf{y}^{(j)}$.

The CG algorithm is not mentioned explicitly as it can be found together with all necessary details of the constrained minimization e.g. in [17].

4 Numerical examples

The present formulation of both solution concepts has been tested numerically.

In the examples presented, there is only one rectangular domain bonded, along its bottom side, to a rigid foundation by a thin adhesive layer. In the first example, the geometry and load configuration are motivated by the pull-push shear test known in several engineering applications. The plane strain problem configuration is shown in Fig. 3. In the second example, the deformed body is the same. Its loading configuration leads to a receding contact after the rupture of the interface, see Fig. 4.

The dimensions of the bulk layer are $L = 250$ mm and $h = 12.5$ mm. It is considered that prior to loading this bulk layer is glued to the support along a part of its bottom side in the extent of $L_c = 225$ mm for the shear test and along the whole bottom side for the contact test, $L_c = L$, for the latter the loading is restricted to a part of the top side with $L_w = 0.3L$. This bulk layer is made of aluminum with Young's modulus $E = 70$ GPa and Poisson's ratio $\nu = 0.35$. The adhesive material is epoxy resin, with Young's modulus $E_e = 2.4$ GPa and Poisson's ratio $\nu_e = 0.33$. Considering the adhesive layer thickness $h_e = 0.2$ mm, the corresponding stiffness parameters are computed following [59] as $k_{\mathbf{n}} = \frac{E_e(1-\nu_e)}{h_e(1+\nu_e)(1-2\nu_e)} = 18\,\mathrm{TPa\,m^{-1}}$ and $\frac{k_{\mathbf{s}}}{k_{\mathbf{n}}} = \frac{1-2\nu_e}{2(1-\nu_e)} = 0.25$.

The parameters that govern the crack growth in the adhesive layer are: the fracture energy in Mode I $G_{\mathrm{d}} = 10\,\mathrm{J\,m^{-2}}$, plastic yield stress $\sigma_{\mathrm{yield}} = 0.56\sqrt{2k_{\mathbf{s}}G_{\mathrm{d}}} = 5.31$ MPa. The hardening slope for plastic slip is $k_{\mathrm{H}} = k_{\mathbf{s}}/9$, the gradient parameters are $k_0 = 10$ μJ and $k_1 = 0\ \mathrm{J\,m^{-2}}$.

The spatial discretization is also the same for both test cases. Four boundary element meshes are used, each with a particular time-step. The coarsest spatial mesh includes a uniform boundary element meshes along the horizontal sides with element length $\ell = 8.333$ mm and two elements along the vertical sides. In this coarsest mesh the time step $\tau = 1.2 \times 10^{-3}$ is used for ES and $\tau = 1.2 \times 10^{-4}$ for MDLS, as it is expected to converge slower. This discretization is

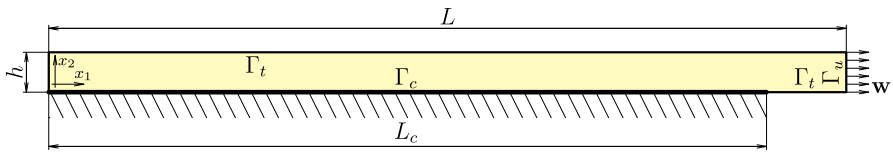

Fig. 3 Geometry for the model of the shear test used in Sect. 4.1

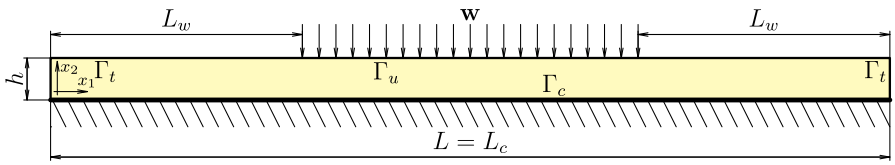

Fig. 4 Geometry for the model of the receding contact used in Sect. 4.2

denoted $N = 30$ according to the number of elements along the bottom side of Γ. The refined meshes are denoted subsequently as $N = 60$, $N = 120$ and $N = 240$: the lengths of all the boundary elements and also the time steps are divided by two with respect to the previous coarser discretization, it means that they are respectively $\tau = 6 \times 10^{-4}, \tau = 3 \times 10^{-4}$ and $\tau = 1.5 \times 10^{-4}$ for ES and $\tau = 6 \times 10^{-5}$, $\tau = 3 \times 10^{-5}$ and $\tau = 1.5 \times 10^{-5}$ for MDLS.

4.1 Shear test

The loading is applied on the right-hand side of the aluminum bulk layer Γ_u, where the prescribed displacements w_1 are increasing during the loading process, whereas $w_2 = 0$. The first-increment of the displacement is given by $w_1^1 = \tau$ mm and it is further multiplied by a factor k equal to the number of the time step changing from an initial value $k = 1$ until the total breakage of the interface occurs.

The process of debonding is controlled by energies, thus a graph of particular energies is shown in Fig. 5.

The total energy consists of both bulk and interface stored energies and also of the energy dissipated which are plotted in the graph. The stored energy has initially quadratic behaviour which changes at points where some plasticity or damage occur. The most apparent change is observable for the first partial debonding—jumps in both stored and dissipated energies. The graph shows that ES makes the structure to break earlier, even the total rupture of the interface in ES occurs before the damage was initialized in MDLS. The first plastic slip appears before the crack initiation, the time of its initiation is observable on the graph by a continuous increase of dissipated energy and appears at the more or less same moment for both solution concepts.

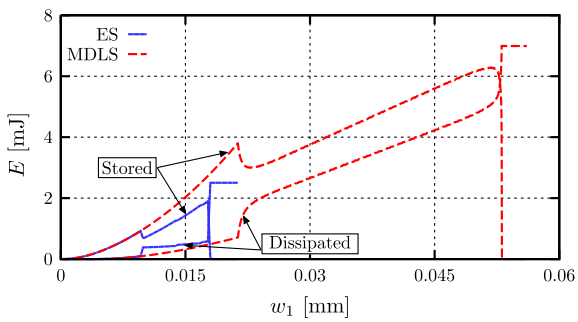

Fig. 5 Energies of both ES and MDLS as functions of time-dependent imposed loading for the finest discretization. In particular, ES ruptures here about 3× earlier than MDLS

The plot in Fig. 6 presents the satisfaction of the two-sided energy inequality (29) which was forced by the BTA of ES and also of the upper estimate in (29) which should be satisfied by MDLS. Here, a better estimation of the energy inequality (24a) for the finer discretizations is evident. The graph in Fig. 6(left) presents ΔE_{est}—the maximum estimated tolerance obtained from (29), formally written in the following way:

$$E_{\text{low}} \le E_{\text{est}} \le E_{\text{up}}, \quad \Delta E_{\text{est}} = \max\big(E_{\text{up}} - E_{\text{est}}, E_{\text{est}} - E_{\text{low}}\big). \tag{54}$$

For MDLS, Fig. 6(right) presents just the difference $E_{\text{up}} - E_{\text{est}}$. As it was expected, the absolute values of the differences are greater for MDLS than for ES as no check on the lower bound, which guaranties the stability of ES, is provided for MDLS, thought with finer discratization the jumps are smaller.

The relation between the resultant reaction force along the adhesive zone and the imposed horizontal displacement is shown in Fig. 7 for the finest discretization. The first sudden decrease of these forces, both horizontal F_1 and vertical F_2, corresponds to the crack initiation—ES breaks earlier then MDLS. After the crack initiation the behaviour of the reaction forces is different. ES provides some hardening, with some partial breaking and an abrupt break of many elements at the end. On the other hand, in MDLS there appears a plateau after the initial break which may represent some stable growth of the interface crack leading to total debonding at the end. In fact, such a behaviour might be expected in view of the related results of pull-

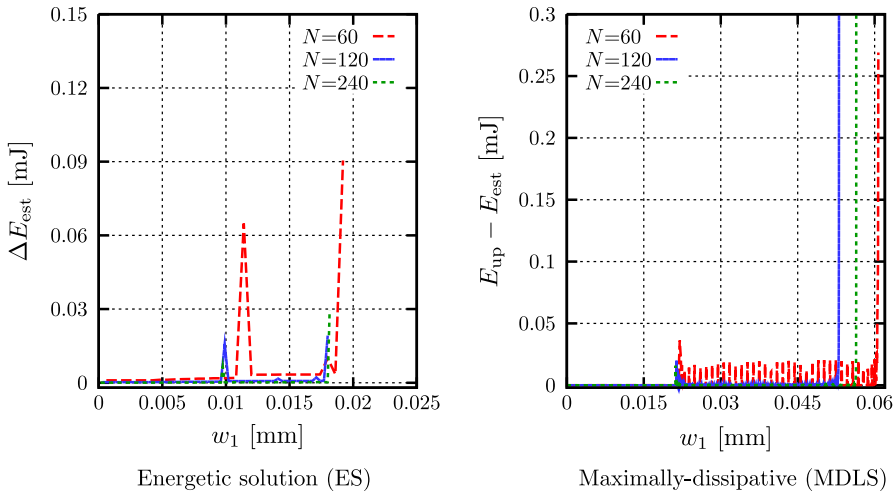

Fig. 6 Convergence, with refining space/time discretization, of error in the energy balance evolving in time (i.e. with respect to loading w_1) for both solution concepts

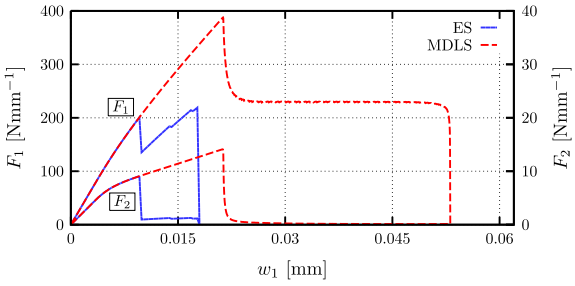

Fig. 7 Resultant force as a function of the imposed displacement for both solution concepts. In particular, ES ruptures here about 3× earlier than MDLS

push shear test [13], see also [45]. The graphs also document onset and increase of plastic slip by a progressive decrease of the slope of the plotted functions. Observing the results of both solution concepts, one can wonder whether the plateau of MDLS can be a continuation of the hardening part in ES which could have been recognized if a full load path had been available.

Figure 8a shows the distributions of displacements and tractions along $\Gamma_{\rm C}$ computed by SGBEM before the crack appears at $k = 32$, for the finest discretization, and right after its initiation at $k = 33$, for ES. The normal u_2 and tangential u_1 displacements are plotted scaled by a factor $k_{\mathbf{n}}$ or $k_{\mathbf{s}}$, respectively, in order to show their linear relation with tractions valid in the elastic range. It is clearly seen that at the end point of the interface a contact zone appears before crack initiation and it also persists in front of the crack tip after the crack initiation. It is the part where the normal displacements are zero and the compressive tractions exhibit a concentration. The tangential components of displacements and tractions do not obey the linear relation in the zone of the plastification in the adhesive layer. It is also clear that after debonding the traction along the pertinent part of $\Gamma_{\rm C}$ vanishes, unless $\Gamma_{\rm C}$ is in contact.

The similar plot is made also for MDLS in Fig. 8b. The distributions of displacements and tractions are presented along $\Gamma_{\rm C}$ before the crack appears at $k = 708$, for the finest discretization, and after its initiation at $k = 718$, for MDLS. Here, due to a smaller time step and not abrupt change of crack length, k was chosen to correspond to a similar time change as plotted for ES. The distributions of the plotted quantities are similar in form though different in magnitudes as for MDLS the crack initiates later.

The next couple of figures documents behaviour of the numerical solution obtained by different discretizations to asses the convergence rate. First, in Fig. 9, there are plotted some detailed parts of the previous distributions of scaled displacements for all but the coarsest discretizations. The curves of all discretizations correspond to the same load, which is either prior to the crack initiation or after the crack initiation in all discretizations, thus e.g. unlike the graphs in Fig. 8 for $N = 120$ the graphs are obtained for $k = 32$ and $k = 40$ for ES, and $k = 704$ and $k = 800$ for MDLS. Before the crack initiation, the plotted curves are the same, beside some approximation differences. After a crack appears, the distributions are different for

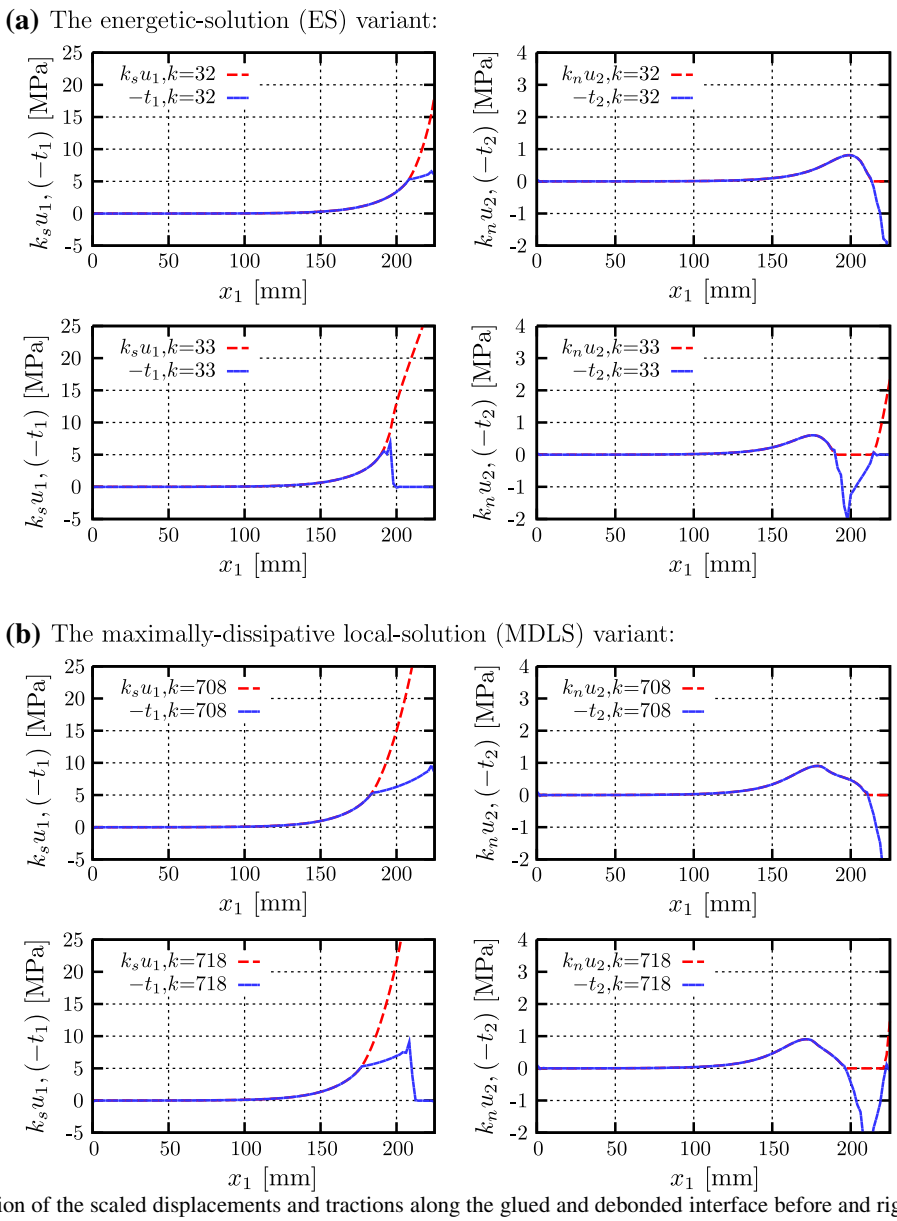

Fig. 8 Distribution of the scaled displacements and tractions along the glued and debonded interface before and right after the crack initiation; the finest discretization is depicted

various discretization though the shape of the curves are similar.

An interesting difference between discretizations and also between ES and MDLS is observed for plastic slip in Fig. 10. For the two finest discretizations with $N = 120$ and $N = 240$ in ES arises another locus of plastic slip after crack initiation, which is not present in the coarser one. The latter is damaged around that locus so that plastic slip is not allowed to evolve. In the MDLS case, however, plasticity was developed more so that on the crack initiation it is evolved in all discretizations. Though the load steps for both ES and MDLS were chosen such that the extent of the damaged interface is similar, the damage evolution in MDLS is more continuous so that also the distribution of plastic slip is smooth, the plateau part of this distribution corresponds to that appeared also in Fig. 7.

The convergence in the case MDLS on Fig. 10 seems to be slower than for ES, although we should

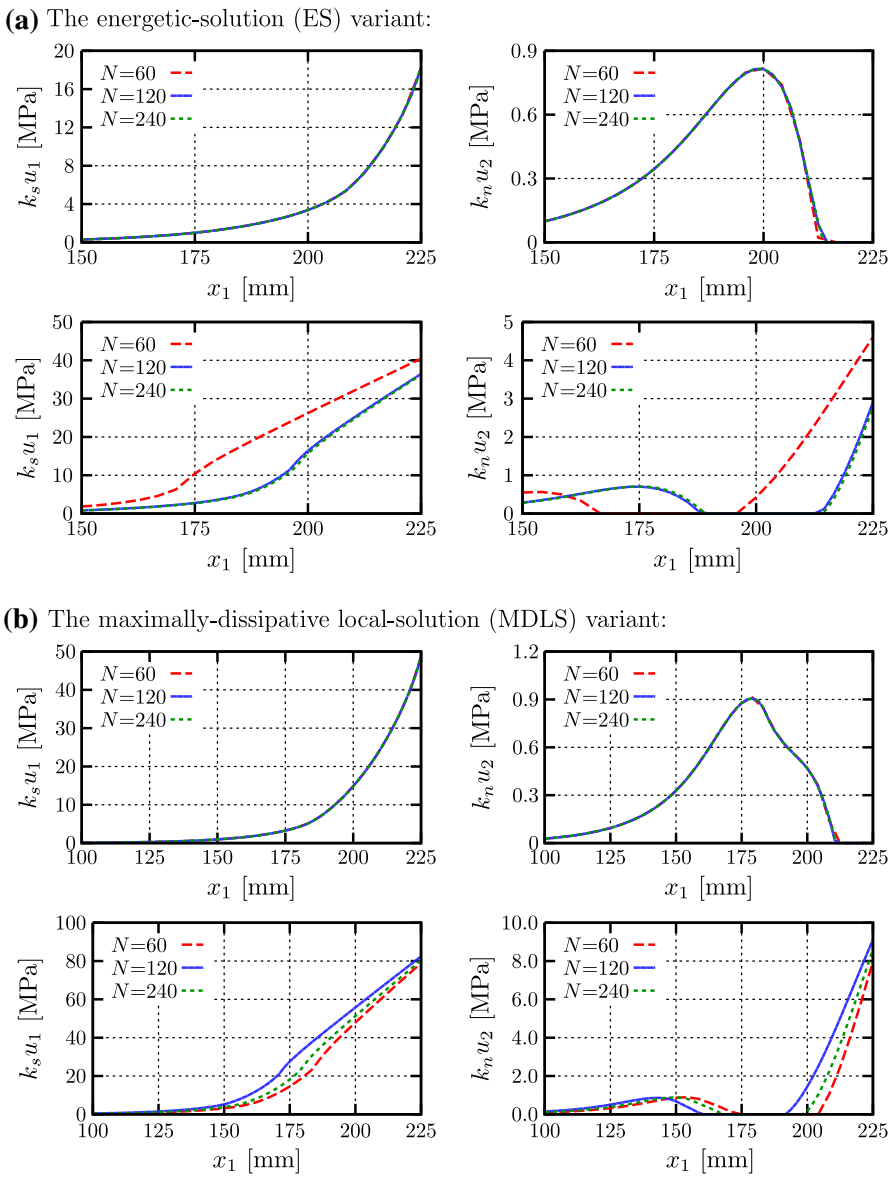

Fig. 9 Convergence, with refining space/time discretization, of the distribution of the scaled displacements along a part of the glued and debonded interface: **a** $w = 9.6$ μm (*top*) and $w = 12$ μm (*bottom*), **b** $w = 21.12$ μm (*top*) and $w = 24$ μm (*bottom*)

emphasize that this convergence is theoretically guaranteed [48]. Anyhow, the fractional-step algorithm (33) works satisfactorily in this example and yields stress-driven local solution (as documented in Fig. 11) delaminating in well pronounced mixed mode (as documented in Fig. 10).

The scaled deformed shape of the bulk layer in ES is shown in Fig. 12a for various load steps in comparison with the original undeformed one. The particular load steps selected are: the first step $k = 1$, the first crack observation (before and after) $k = 32$ and $k = 33$ (valid for the finest discretization), and all successive crack-length changes (before and after) until the total debonding of Γ_C at the load-step $k = 60$.

A similar plot is made also for MDLS in Fig. 12b. The scale factor for the displacements is chosen the same for both solution concepts and is equal to 2000. Recall also that the time step for MDLS is ten times less than for ES so that e.g. $k = 60$ for ES corresponds to $k = 600$ for MDLS. The particular load steps

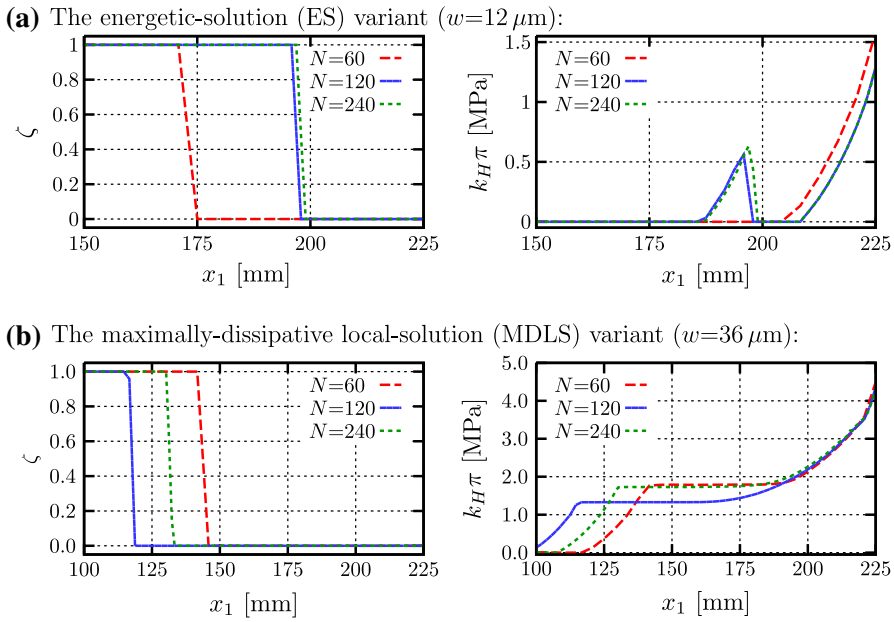

Fig. 10 Convergence, with refining space/time discretization, of distribution of the damage parameter ζ and plastic slip π along a part of the glued and debonded interface. In particular, comparing the plastic slip π, it can also be seen that ES has delaminated (rather nonphysically) mostly in less dissipative Mode I while MDLS executed delamination in truly mixed mode

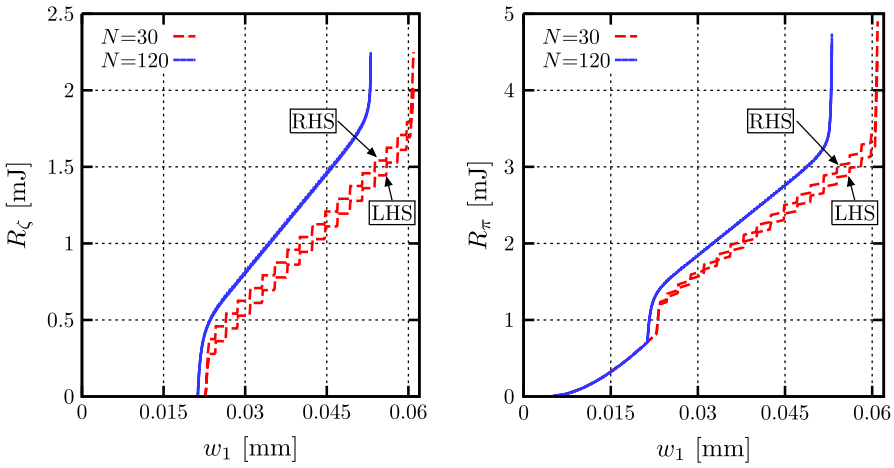

Fig. 11 Satisfaction of the approximate maximum-dissipation principle (36a) (*left*) and (36b) (*right*) for two discretizations; on the finer discretization, the differences between the left-hand side (LHS) and the right-hand side (RHS) of (36) are not visible and the approximate MDLS is thus very well stress-driven

selected are: the first step $k = 1$, the first crack observation (before and after) $k = 710$ and $k = 711$ (valid for the finest discretization), some intermediate load step for $k = 1{,}200$, and three load steps from the end of the history, namely $k = 1{,}762$, $k = 1{,}767$ and $k = 1{,}768$, the total debonding which occurred in the next step is not plotted. Here, we can see continuous evolution of the interface crack and also an effect of peeling close to the end of the load history before the total damage occurred.

Finally, the influence of the gradient-of-damage coefficients is worth to be numerically studied. Yet, the effects are quite expectable so we present it only for k_0 (as actually we neglected k_1 in our calculations). The parameter tends to regularize the solution so that at each interface point the damage grows less abruptly and in a way can affect the smoothness of a crack propagation. More specifically, the coefficient k_0, so far considered 10 μJ, is now varied as 1 μJ, 100 μJ, and 10 mJ. The graphs in Fig. 13 concern the case MDLS and show the resultant interface forces for the three new values of k_0. Before the initiation of the damage, all three graphs coincide. Then the higher value of k_0 causes the later initiation of rupture but

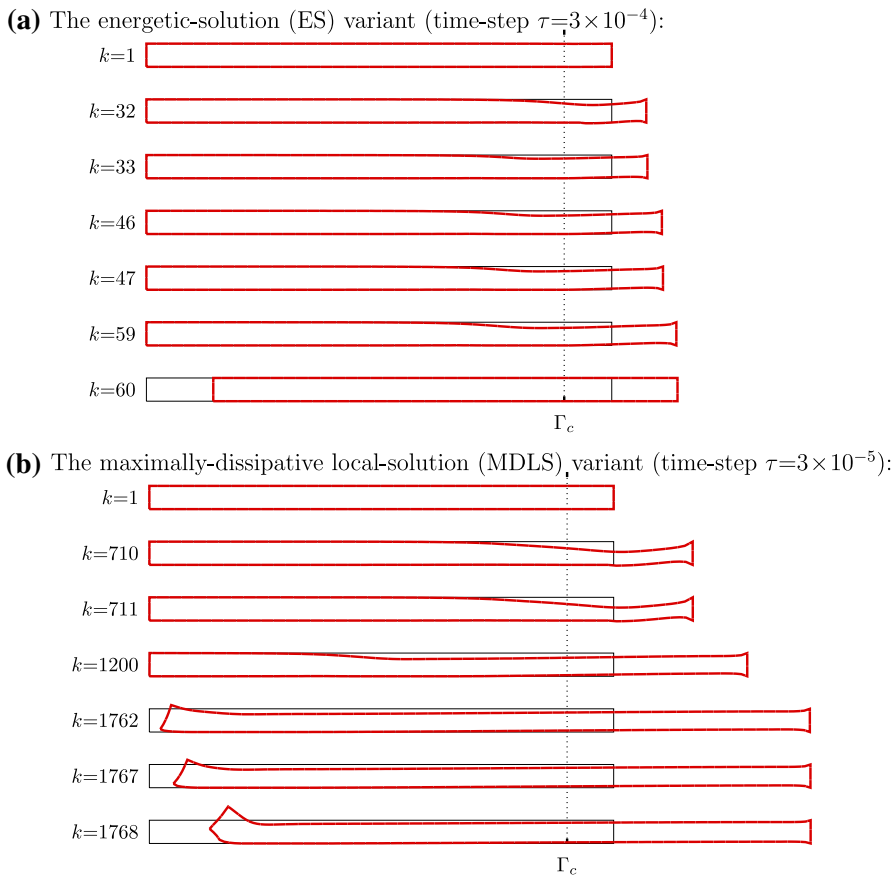

Fig. 12 Deformed and the undeformed original shapes of the bulk layer for seven selected time instants and the finest discretization. ES ruptures here about 3× earlier than stress-driven MDLS, cf. also Figs. 5 and 7. Displacement depicted magnified 2,000×

simultaneously lower level of the plateau and earlier total breakage. The smoothness of the damage response can be clearly observed in Fig. 14. The graphs correspond to the imposed displacement $w_1 = 32$ μm, for which the interface is partially but not totally damaged for all k_0. The distribution of ζ for small k_0 contains an abrupt fall from one to zero, while for the greatest k_0 the distribution is relatively smooth. This also influences the distribution of plastic slip which tends to have less abrupt variations in its values along the whole interface.

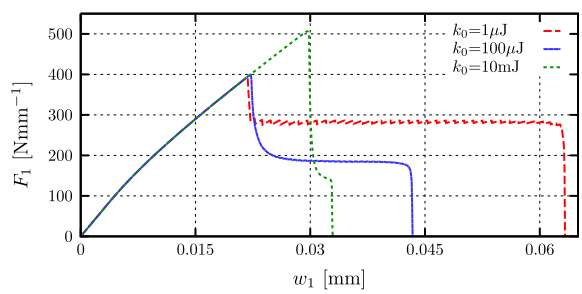

Fig. 13 Resultant horizontal force as a function of the imposed displacement for various values of the gradient-of-damage coefficient k_0 calculated for MDLS

4.2 Debonding with receding contact

The load, in the form of prescribed displacements, is applied on a part of the top side of the aluminum bulk layer Γ_u. The prescribed displacements are increasing during the loading process. The first-increment of loading is given by $w_2^1 = -\tau$ mm and $w_1^1 = 0$ again with $\tau = 1.2 \times 10^{-3}$ for ES and with $\tau = 1.2 \times 10^{-4}$ for MDLS, and it is further multiplied by a factor k. The three discretizations, both in time and space, as in the previous example are used, in particular $N = 30$, $N = 60$ and $N = 120$.

The process of debonding is controlled by energies, thus graphs of stored-in-adhesive and dissipated energies are shown in Fig. 15. In the loading process,

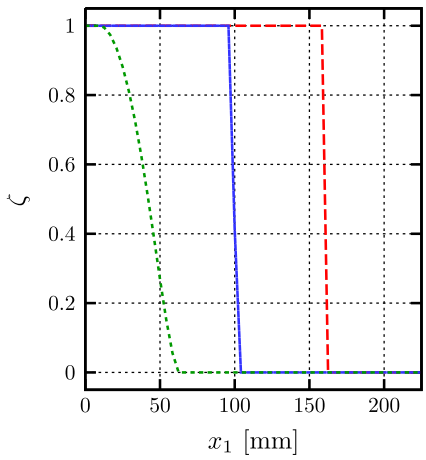

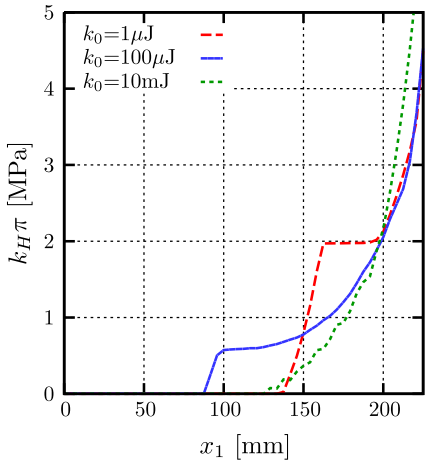

Fig. 14 Distribution of the damage parameter ζ and plastic slip π along Γ_C for various values of the gradient-of-damage coefficient k_0 at one selected time instant calculated for MDLS

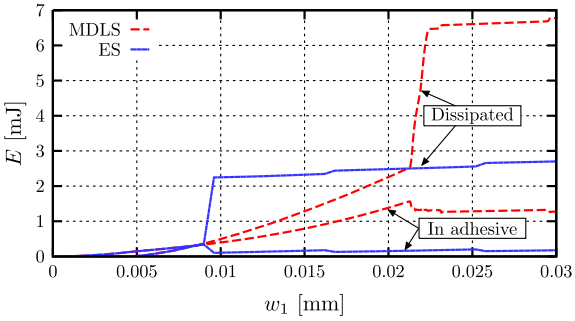

Fig. 15 Evolution of energies of both ES and MDLS as functions of time-dependent loading for the finest discretization. In particular, ES ruptures here about 2× earlier than MDLS

a large amount of the energy is stored in the bulk. This energy is not influenced too much by the rupture of the interface and is not plotted here for the sake of clarity. Nevertheless, the energy stored in the adhesive changes significantly, together with the energy dissipated.

The ES case exhibits a too early debonding which in fact, as will be seen later, does not cover the all expected evolution of debonding. The energy releases step-wise from the adhesive at the moments of some crack length increase and releases continuously with the evolution of plastic slip. In this type of loading, it might be difficult to make the total damage of the interface adhesive as the prescribed displacements is only vertical, keeping the zero horizontal displacement at the top side of the bulk layer. For finer meshes, it took a lot of time-steps to meet the conditions of the total rupture—the curve for the finest mesh evolve far behind the breakage point of the coarser ones. In the continuous case, the midpoint of the interface never

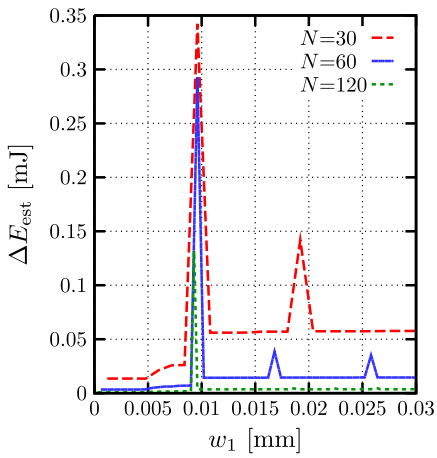

Energetic solution (ES)

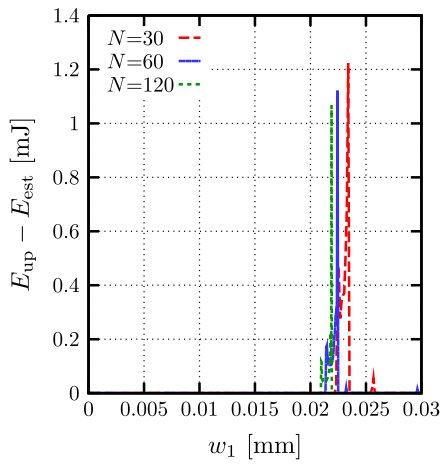

Maximally-dissipative (MDLS)

Fig. 16 Convergence, with refining space/time discretization, of the error in the energy balance as a function of time (through the loading w_1) for both solution concepts

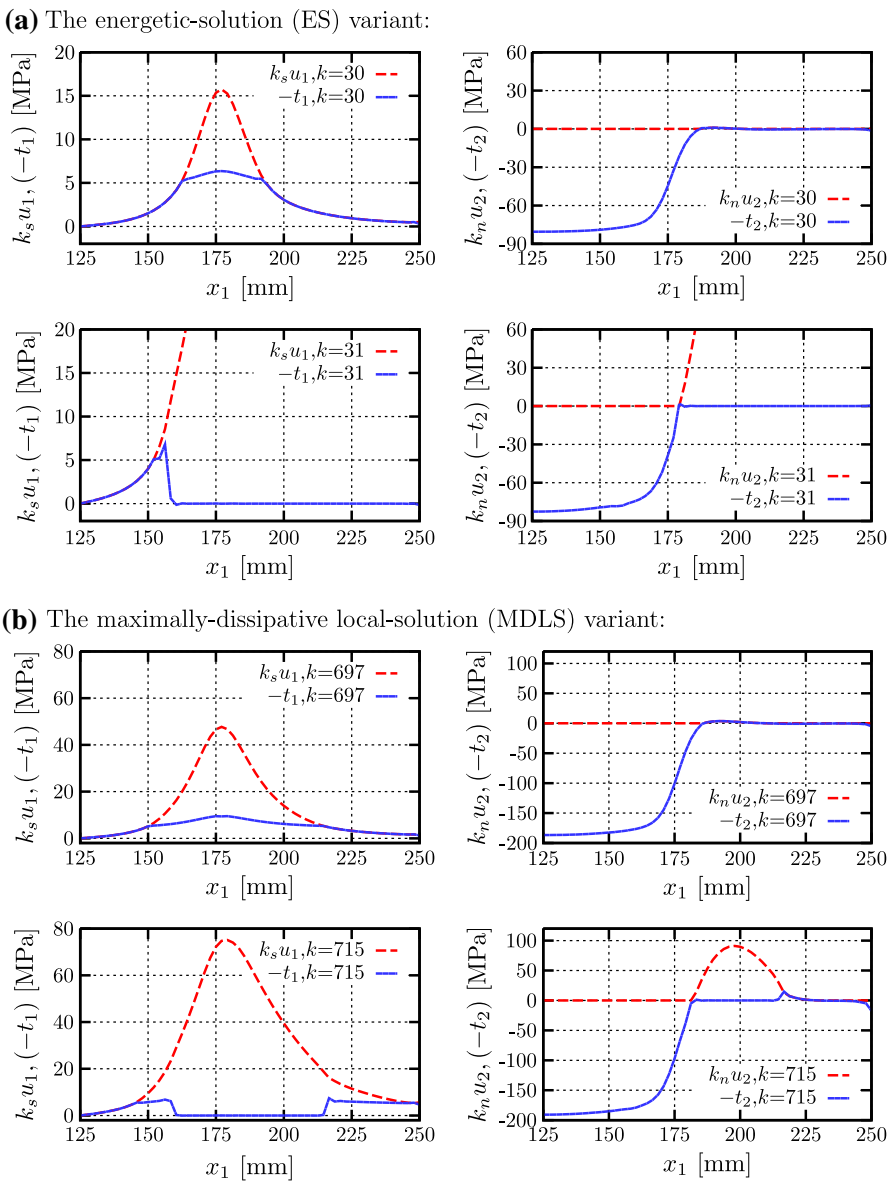

Fig. 17 Distribution of scaled displacements and tractions along the glued and debonded interface before and right after the crack initiation; the finest discretization is used

breaks. Thus, only a part of the load history is plotted which essentially includes the debonding of the lateral not loaded parts of the bulk layer.

Figure 16 shows the energy tolerances provided by the energy estimate (54) for ES and by difference $E_{\text{up}} - E_{\text{est}}$ for MDLS. A decreasing variation in the energy estimation bounds for finer discretizations and sharp peaks of these tolerances at the instants of sudden changes at the interface can be observed. The difference is naturally greater for the MDLS concept.

Let us look at the interface displacements and tractions obtained by the finest discretization shown in Fig. 17. The results are symmetric so only a half of the interface for $x_1 \geq 125$ mm is shown. The first crack appears for $k = 31$ ($w_2^{31} = 9.3 \times 10^{-3}$ mm) in ES and in fact the whole not loaded part of the bulk layer is released. Figure 17a shows the distributions of the scaled displacements and tractions along Γ_C before the crack appears, $k = 30$, and right after its initiation. It is clear that below Γ_u, where displacements are prescribed (the end point of Γ_u is at $x_1 = 175$ mm) compressive stresses appear in the adhesive. Close to this zone, a small area of tensile loading can be observed before originating a crack, see also the detail

in Fig. 18, farther from this area the deformation decreases. The crack initiation and evolution is abrupt—the problem suddenly changes to a receding-contact phenomenon. This change is surprising because there were almost no tractions at the end points of the bulk layer. This could be understood recalling the character of ES—it is a global minimum, or its approximation.

It is interesting to observe also the tangential components. Close to the end point of Γ_u, the plastification in the adhesive developed before the crack appears—the tangential components do not obey the linear relation in this zone. After debonding, the traction along the debodned part of Γ_C vanishes, unless Γ_C is in contact—this is the difference in the extent of the vanishing tangential and normal tractions in the bottom pictures in both Fig. 17a, b.

In the ES case, some part of the deformation history evidently misses, but this part was, however, found by MDLS. In the latter case, the crack was initiated below the endpoint of the load for $k = 697$ ($w_2^{697} = 0.02091$ mm) and grows until $k = 730$ ($w_2^{730} = 0.0219$ mm) when the unloaded part of the bulk layer is released. Figure 17b shows the distributions of the

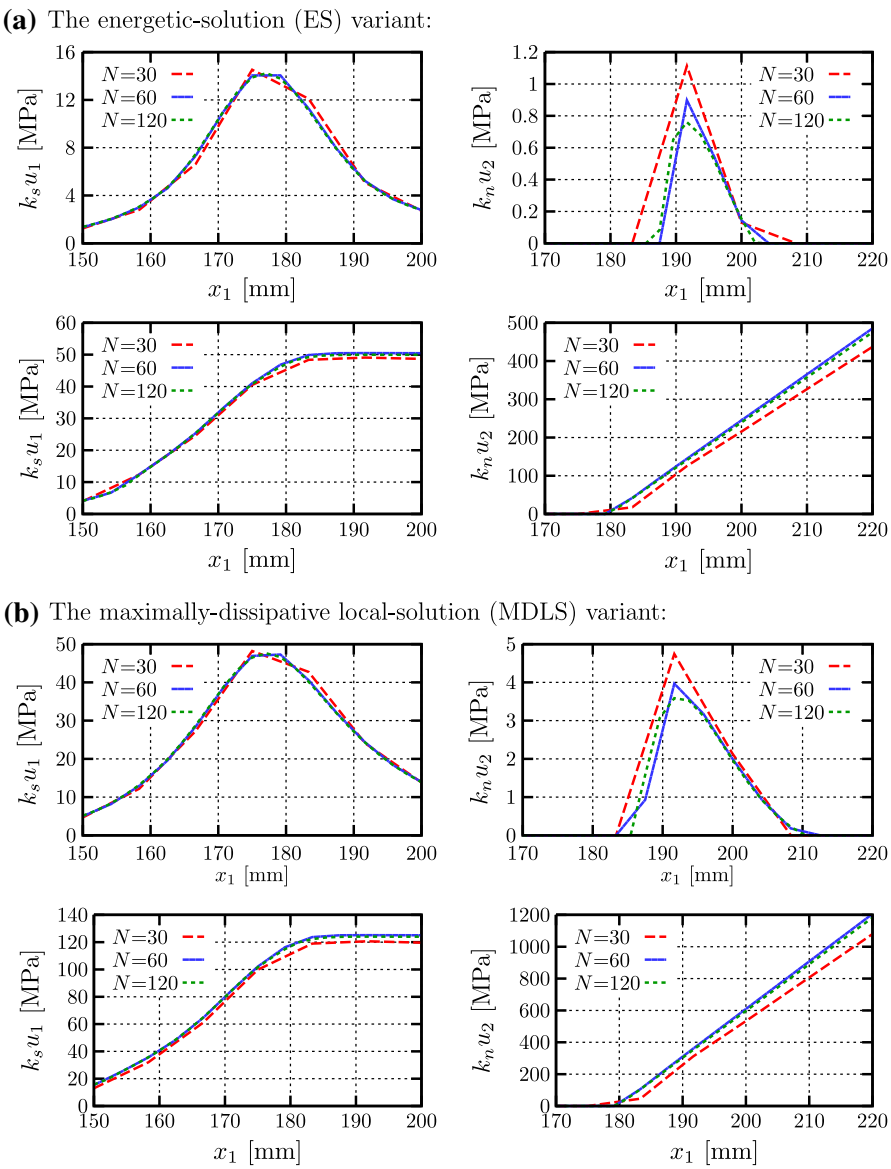

Fig. 18 Convergence, with refining space/time discretization, of the distribution of displacements along a part of the glued and debonded interface: **a** $w = 8.4$ µm (*top*) and $w = 9.6$ µm (*bottom*), **b** $w = 20.88$ µm (*top*) and $w = 23.4$ µm (*bottom*)

scaled displacements and tractions along Γ_C before the crack appears, $k = 697$, and at some intermediate time step $k = 715$. The difference between these two k in fact corresponds to the time step used in the ES case. Here, it is clear from the graphs that the crack extends along a part of the interface where tractions are zero and normal displacements u_2 are positive. The presence of the plastification at the end part of the bulk layer ($x_1 \geq 225$) is evident as the linear relation between scaled tangential displacement and traction is not satisfied but the relation between the normal components still holds.

Some aspects of the convergence with the discretization refinement are illustrated in Figs. 18 and 19. Compared to the previous example in Sect. 4.1, the convergence for the used meshes is observed also after the crack onset, the difference between finer meshes is smaller than between coarser meshes with no difference for MDLS case. In particular, Fig. 18, shows the distribution of the displacements in a part of the bottom side of the bulk layer. In the plots, the load steps are taken such that for none of the discretizations a crack appears—the top plots in both Fig. 18a, b, or the interface is broken for all the discretizations—the bottom plots. The distribution of the plotted functions is really similar, as it can be observed for convergent solutions. According to the above, a small area of tensile stretch is shown before the damage initiation. Though not the same in magnitude, the shape of distribution of displacements is similar both for ES and for MDLS.

Figure 19 shows the state of damage and distribution of plastic slip for a later time step, in fact for both solution concepts the same imposed displacement is applied though of course at different time steps. As expected, the damage usually achieves only one of the limit values: undamaged '1' or fully damaged '0'. There is no difference for all the three discretizations. Nevertheless, the plastic slip smoothes out for the finer discretizations. Two hats in the distribution for ES appear due to the step-wise breakage of the interface. The first crack included the whole plastic zone developed prior to the crack initiation (the right hat) whose evolution has stopped after damage. Later, another evolving plastic zone appeared (the left hat), compare with Fig. 17a. In the MDLS case the crack length increases continuously and never goes beyond the plastic region so that the distribution of plastic slip is not split into two parts.

As we mentioned in the previous example, it is difficult (and even not always automatic) to guarantee the convergence in the MDLS case towards truly stress-driven local solutions. Therefore, it is again worth checking a-posteriori approximate maximum dissipation principle (36). Like in the previous example in Fig. 11, now Fig. 20 shows the differences in (36). The differences are however greater then in the previous example, which is not much surprising

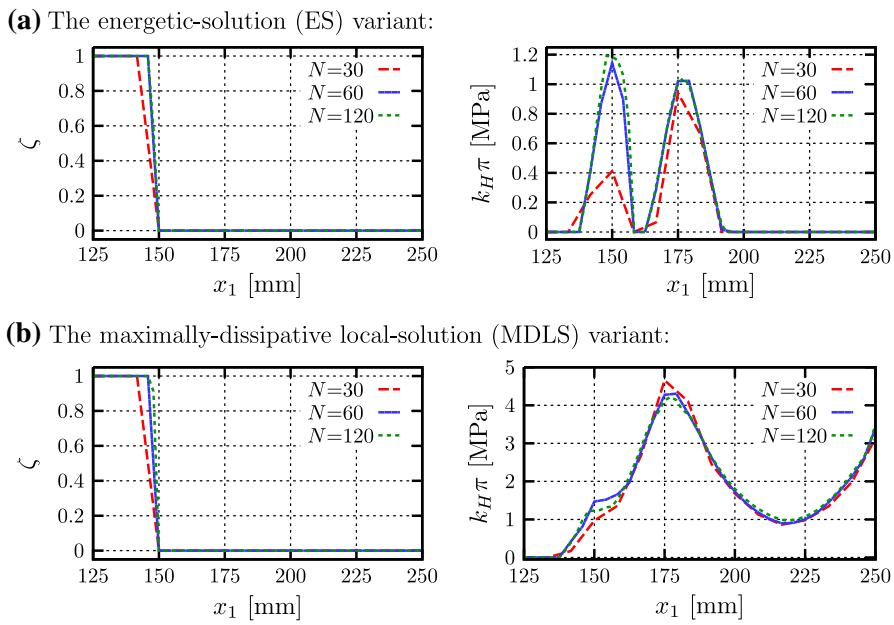

Fig. 19 Convergence, with refining space/time discretization, of the distribution of the damage parameter ζ and scaled plastic slip π along a part of the glued and debonded interface for $w = 30$ μm

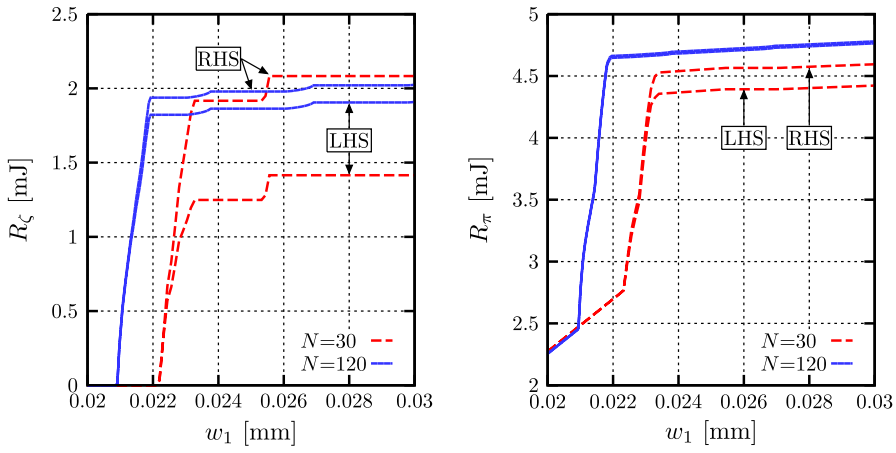

Fig. 20 Satisfaction of the approximate maximum-dissipation principle (36a) (*left*) and (36b) (*right*) for two discretizations

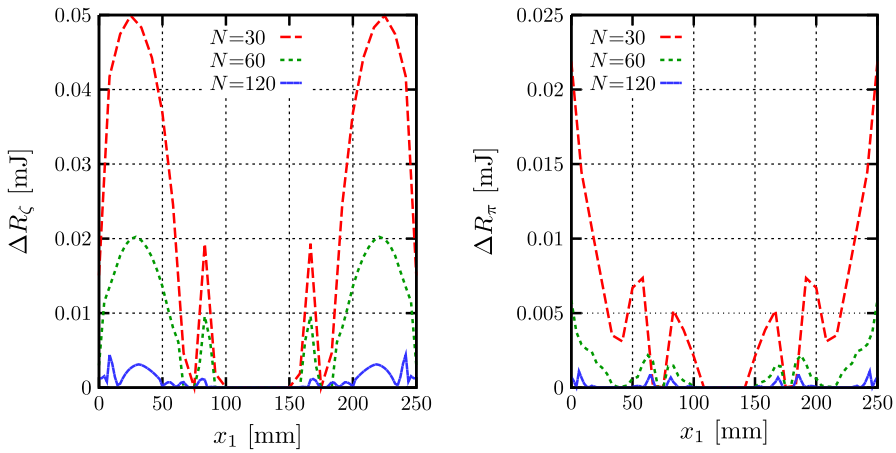

Fig. 21 Convergence, with refining space/time discretization, of the integrands in (55), documenting spatial distribution along Γ_C of the numerical error of the approximate Hill maximum dissipation principle for the damage parameter ζ (*left*) and plastic slip π (*right*)

because this example exhibits clear tendency of delaminating bigger portion of Γ_C at once and then some rupture may happen under sub-critical driving force and the maximum-dissipation principle may tend to be not completely satisfied, even though it need not be related to unphysically too-early ruptures. This is therefore an interesting example where these effects seem to be slightly visible and it is worth observing spatial distribution along Γ_C of the residua in AMDP (37) counted for $t = T$ to see where this possible deviation from the IMDP occurred. To this goal, we can re-write AMDP (37) as:

$$\Delta R_{\zeta,\tau}(T) = \int_{\Gamma_C} \left(G_d(\zeta_\tau^K - \zeta_0) - \sum_{k=1}^{T/\tau} f_\tau^{k-1}(\zeta_\tau^k - \zeta_\tau^{k-1}) \right) \mathrm{d}S,$$
$$f_\tau^k \in -\partial_\zeta \mathcal{E}(u_\tau^k, \zeta_\tau^{k-1}, \pi_\tau^k), \tag{55a}$$

$$\Delta R_{\pi,\tau}(T) =$$
$$\int_{\Gamma_C} \left(\sum_{k=1}^{T/\tau} \sigma_{\text{yield}} \left| \pi_\tau^k - \pi_\tau^{k-1} \right| - g_\tau^{k-1}(\pi_\tau^k - \pi_\tau^{k-1}) \right) \mathrm{d}S,$$
$$g_\tau^k \in -\partial_\pi \mathcal{E}(u_\tau^k, \zeta_\tau^k, \pi_\tau^k), \tag{55b}$$

and we can then display the integrands in (55) as a function of $x \in \Gamma_C$. This is done in Fig. 21 even for three different discretizations, but it seems to reveal quite nice numerical convergence so that, expectedly, the maximum-dissipation principle is well satisfied even in this relatively sophisticated experiment. Again, it documents that the fractional-step-type algorithm (33) efficiently calculated stress-driven local solution.

Finally, the scaled deformed shape of the bulk layer is shown in Fig. 22 for various load steps and the finest

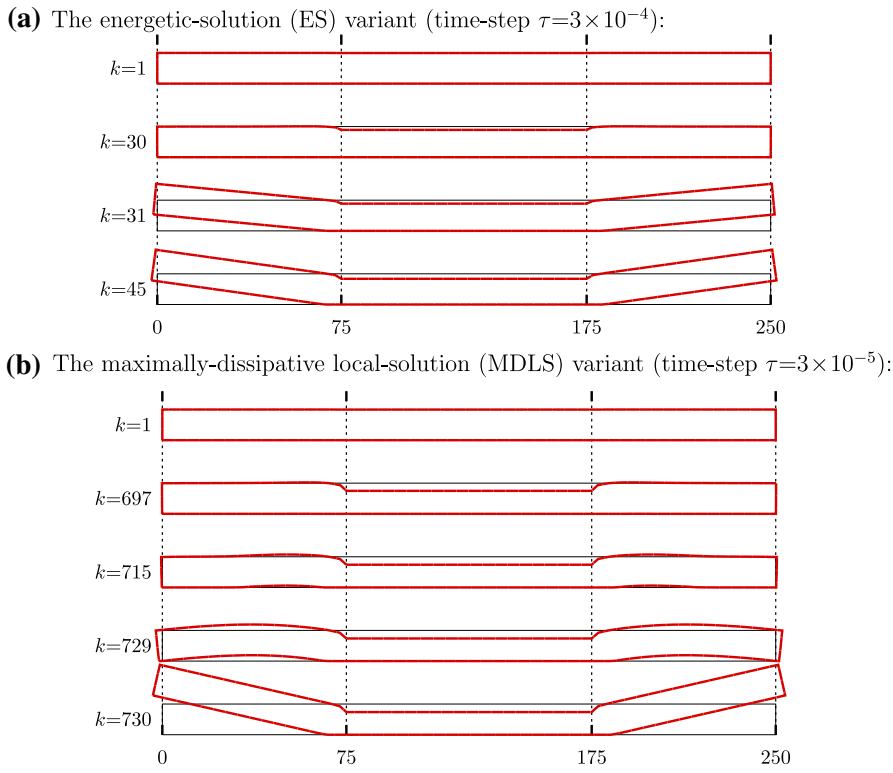

Fig. 22 Deformed and the undeformed original undeformed shapes of the bulk layer for various time instances and the finest discretization. ES ruptures here about 2× earlier than the stress-driven (i.e. MDLS) one, cf. also Fig. 15. Displacement depicted magnified 150×

discretization in comparison with the original undeformed one. The particular load steps selected for ES are: the first step $k = 1$, the first crack observation (before and after) $k = 30$ and $k = 31$ and a successive crack length change $k = 45$. The total debonding of Γ_C which occured at the load-step $k = 1{,}695$ is not plotted as it seems physically unrealistic. For MDLS the plotted data correspond to: the first step $k = 1$, the step right before the first crack observation $k = 697$, an intermediate state for $k = 715$ and two time steps $k = 729$ and $k = 730$ which correspond to debonding of the whole not loaded part, just before and after, respectively. As mentioned above, the loading causes receding contact after debonding.

5 Conclusions

An energy-based model for interface debonding with a fracture-mode-sensitive crack growth under rate-independent conditions has been considered. The sensitivity of the model to opening Mode I and shearing Mode II cracks has been achieved by considering two internal variables along the interface: damage parameter ζ and plastic slip π, the latter being inactive in Mode I. The numerical implementation of spatial discretization via SGBEM has permitted the whole problem to be defined only by the boundary and interface data. Two solution concepts have been applied and compared in the numerical analysis: The energy-conserving concept of energetic solution (ES) and a stress-driven, maximally-dissipative local-solution concept (MDLS). Simple two-dimensional examples have validated the model and have shown that it provides expected results: typically, due to ES's search for global minimizers of the energetic functional, they may rupture earlier under less work of external loading (thus dissipating less energy, exhibiting sometimes unphysical tendency to prefer less dissipative Mode I) than MDLS's. Examples of such not entirely realistic responses are on Fig. 12a and 22a. While for the used MDLS concept, some of the expected responses have been achieved together with a-posteriori validation of (an approximate variant of an integrated version of) the Hill's maximum-dissipation principle. Another possibility of elimination or reducing of the undesired attributes of ES includes adding a small viscosity similarly as in [42] for mixed-

mode insensitive variant, although it is computationally very difficult to obtain as documented in [45], and is intended to discuss it in future releases.

Acknowledgments The authors are indebted to an anonymous reviewer for many useful suggestions that improved the presentation in particular aspects. A part of the work has been accomplished during the stages of R. V. and T. R. at Universidad de Sevilla whose hospitality is acknowledged. Moreover, the authors acknowledge the support from the Spanish Ministry of Education (Ref. SAB2010-0082) and Spanish Ministry of Economy and Competitiveness (Project MAT2012-37387), from the Junta de Andalucía and European Social Fund through the Project of Excellence P08-TEP-04051, from the Slovak Ministry of Education through the grant 1/0201/11 (VEGA), as well as from the Czech Republic through the grants 201/10/0357, 201/12/0671, and 105/13/18652S (GA ČR), together with the institutional support RVO: 61388998.

References

1. Alfano G, Sacco E (2006) Combining interface damage and friction in a cohesive-zone model. Int J Numer Methods Eng 68:542–582
2. Allix O, Feld N, Baranger E, Guimard J-M, Ha-Minh C (2014) The compressive behaviour of composites including fiber kinking: modelling across the scales. Meccanica. doi:10.1007/s11012-013-9872-y
3. Banks-Sills L, Ashkenazi D (2000) A note on fracture criteria for interface fracture. Int J Fract 103:177–188
4. Bartels S, Kružík M (2011) An efficient approach to the numerical solution of rate-independent problems with nonconvex energies. Multiscale Model Simul 9:1276–1300
5. Benešová B (2011) Global optimization numerical strategies for rate-independent processes. J Glob Optim 50:197–220
6. Bonnet M (1995) Regularized direct and indirect symmetric variational BIE formulations for three-dimensional elasticity. Eng Anal Bound Elem 15:93–102
7. Bonnet M, Maier G, Polizzotto C (1998) Symmetric Galerkin boundary element method. Appl Mech Rev 15:669–704
8. Bourdin B (2007) Numerical implementation of the variational formulation for quasi-static brittle fracture. Interfaces Free Bound 9:411–430
9. Bourdin B, Francfort A, Marigo JJ (2000) Numerical experiments in revisited brittle fracture. J Mech Phys Solids 48:797–826
10. Bourdin B, Francfort A, Marigo JJ (2008) The variational approach to fracture. J Elasticity 91:5–148
11. Carpinteri A (1989) Cusp catastrophe interpretation of fracture instability. J Mech Phys Solids 37:567–582
12. Carpinteri A, Cornetti P, Pugno N (2009) Edge debonding in FRP strengthtened beams; stress versus energy failure criteria. Eng Struct 21:2436–2447
13. Cornetti P, Carpinteri A (2011) Modelling of FRP-concrete delamination by means of an exponentially softening law. Eng Struct 33:1988–2001
14. Cornetti P, Mantič V, Carpinteri A (2012) Finite fracture mechanics at elastic interfaces. Int J Solids Struct 49:1022–1032
15. Dal Maso G, Francfort GA, Toader R (2005) Quasistatic crack growth in nonlinear elasticity. Arch Rational Mech Anal 176:165–225
16. Diaz-Diaz A, Caron J-F (2006) Interface plasticity and delamination onset prediction. Mech Mater 38:648–663
17. Dostál Z (2009) Optimal quadratic programming algorithms. Springer, Berlin
18. Evans A, Rühle M, Dalgleish B, Charalambides P (1990) The fracture energy of bimaterial interfaces. Metall Trans A 21A:2419–2429
19. Frémond M (1985) Dissipation dans l'adhérence des solides. CR Acad Sci Paris Ser II 300:709–714
20. Frémond M (2002) Non-smooth thermomechanics. Springer, Berlin
21. Giambanco G, Scimemi GF (2006) Mixed mode failure analysis of bonded joints with rate-dependent interface models. Int J Numer Methods Eng 67:1160–1192
22. Grassl P, Rempling R (2008) A damage-plasticity interface approach to the meso-scale modelling of concrete subjected to cyclic compressive loading. Engng Fract Mech 75:4804–4818
23. Hill R (1948) A variational principle of maximum plastic work in classical plasticity. Q J Mech Appl Math 1:18–28
24. Hutchinson JW, Suo Z (1992) Mixed mode cracking in layered materials. Adv Appl Mech 29:63–191
25. Kočvara M, Mielke A, Roubíček T (2006) A rate-independent approach to the delamination problem. Math Mech Solids 11:423–447
26. Kolluri M, Hoefnagels JPM, van Dommelen JAW, Geers MGD (2011) An improved miniature mixed-mode delamination setup for in situ microscopic interface failure analyses. J Phys D Appl Phys 44:034005
27. Kolluri M, Hoefnagels JPM, van Dommelen JAW, Geers MGD (2013) A practical approach for the separation of interfacial toughness and structural plasticity in a delamination growth experiment. Int J Fract 183:1–18
28. Lenci A (2001) Analysis of a crack at a weak interface. Int J Fract 108:275–290
29. Liechti K, Chai Y (1992) Asymmetric shielding in interfacial fracture under in-plane sheare. J Appl Mech 59:295–304
30. Mantič V (2008) Discussion on the reference length and mode mixity for a bimaterial interface. J Eng Mater Technol 130:045501-1-2
31. Mantič V, Távara L, Blázquez A, Graciani E, París F (2013) Application of a linear elastic–brittle interface model to the crack initiation and propagation at fibre–matrix interface under biaxial transverse loads. ArXiv preprint. arXiv:1311.4596.
32. Matzenmiller A, Gerlach S, Fiolka M (2010) A critical analysis of interface constitutive models for the simulation of delamination in composites and failure of adhesive bonds. J Mech Mater Struct 5:185–211
33. Mielke A (2011) Differential, energetic and metric formulations for rate-independent processes. In: Ambrosio L, Savaré G (eds) Nonlinear PDEs and applications. Springer, Heidelberg, pp 87–170
34. Mielke A, Roubíček T (2015) Rate-independent systems—theory and application. Applied Mathematical Sciences Series. Springer, New York (contracted)

35. Mielke A, Theil F (2004) Mathematical model for rate-independent phase transformations with hysteresis. Nonlinear Differ Equ Appl 11:151–189
36. Mielke A, Roubíček T, Zeman J (2010) Complete damage in elastic and viscoelastic media and its energetics. Comput Methods Appl Mech Eng 199:1242–1253
37. Moreo P, García-Aznar JM, Doblaré M (2007) A coupled viscoplastic rate-dependent damage model for the simulation of fatigue failure of cement-bone interfaces. Int J Plasticity 23:2058–2084
38. Panagiotopoulos CG, Mantič V, Roubíček T (2013) BEM implementation of energetic solutions for quasistatic delamination problems. Comput Mech 51:505–521
39. París F, Cañas J (1997) Boundary element method. Fundamentals and applications. Oxford University Press, Oxford
40. Roubíček T (2009) Rate independent processes in viscous solids at small strains. Math Methods Appl Sci 32:825–862 (Erratum 2176)
41. Roubíček T (2013) Nonlinear partial differential equations with applications, 2nd edn. Birkhäuser, Basel
42. Roubíček T (2013) Adhesive contact of visco-elastic bodies and defect measures arising by vanishing viscosity. SIAM J Math Anal 45:101–126
43. Roubíček T (submitted) Maximally-dissipative local solutions to rate-independent systems and application to damage and delamination problems. Nonlinear Anal
44. Roubíček T, Mantič V, Panagiotopoulos C (2013) Quasistatic mixed-mode delamination model. Discr Contin Dyn Syst 6:591–610
45. Roubíček T, Panagiotopoulos C, Mantič V (2013) Quasistatic adhesive contact of visco-elastic bodies and its numerical treatment for very small viscosity. Z Angew Math Mech 93:823–840
46. Roubíček T, Scardia T, Zanini C (2009) Quasistatic delamination problem. Contin Mech Thermodyn 21: 223–235
47. Roubíček T, Kružík M, Zeman J (2014) Delamination and adhesive contact models and their mathematical analysis and numerical treatment. In: Mantič V (ed) Mathematical methods and models in composites. Imperial College Press, London, pp 349–400
48. Roubíček T, Panagiotopoulos C, Mantič V (submitted) Local-solution approach to quasistatic rate-independent mixed-mode delamination. Math Models Methods Appl Sci
49. Sauter SA, Schwab C (2010) Boundary element methods. Springer, Berlin
50. Scheider I (2009) Derivation of separation laws for cohesive models in the course of ductile fracture. Eng Fract Mech 76:1450–1459
51. Scheider I, Mosler J (2011) Novel approach for the treatment of cyclic loading using a potential-based cohesive zone model. Procedia Eng 10:2164–2169
52. Sirtori S (1979) General stress analysis by means of integral equations and boundary elements. Meccanica 14:210–218
53. Sirtori S, Miccoli S, Korach E (1993) Symmetric coupling of finite elements and boundary elements. In: Kane JH, Maier G, Tosaka N, Atluri SN (eds) Advances in boundary element techniques. Springer, Berlin, pp 407–427
54. Snozzi L, Molinari J-F (2013) A cohesive element model for mixed mode loading with frictional contact capability. Int J Numer Methods Eng 93:510–526
55. Spada A, Giambanco G, Rizzo P (2009) Damage and plasticity at the interfaces in composite materials and structures. Comput Methods Appl Mech Eng 198:3884–3901
56. Stefanelli U (2009) A variational characterization of rate-independent evolution. Math Nach 282:1492–1512
57. Sutradhar A, Paulino GH, Gray LJ (2008) The symmetric Galerkin boundary element method. Springer, Berlin
58. Swadener J, Liechti K, deLozanne A (1999) The intrinsic toughness and adhesion mechanism of a glass/epoxy interface. J Mech Phys Solids 47:223–258
59. Távara L, Mantič V, Graciani E, París F (2011) BEM analysis of crack onset and propagation along fiber–matrix interface under transverse tension using a linear elastic-brittle interface model. Eng Anal Bound Elem 35:207–222
60. Toader R, Zanini C (2009) An artificial viscosity approach to quasistatic crack growth. Boll Unione Matem Ital 2:1–36
61. Vodička R, Mantič V, París F (2007) Symmetric variational formulation of BIE for domain decomposition problems in elasticity—an SGBEM approach for nonconforming discretizations of curved interfaces. CMES Comput Model Eng 17:173–203
62. Vodička R, Mantič V, París F (2011) Two variational formulations for elastic domain decomposition problems solved by SGBEM enforcing coupling conditions in a weak form. Eng Anal Bound Elem 35:148–155
63. Xu Q, Lu Z (2013) An elastic–plastic cohesive zone model for metal-ceramic interfaces at finite deformations. Int J Plasticity 41:147–164
64. Ziegler H (1958) An attempt to generalize Onsager's principle, and its significance for rheological problems. Z Angew Math Phys 9b:748–763